

1 **An assessment of land energy balance over East Asia from**
2 **multiple lines of evidence and the roles of Tibet Plateau,**
3 **aerosols, and clouds**

4
5 Qiuyan Wang^{1,2,6}, Hua Zhang^{1,2}, Su Yang³, Qi Chen², Xixun Zhou², Bing Xie⁴, Yuying
6 Wang¹, Guangyu Shi^{1,5}, Martin Wild⁶

7
8 ¹ Collaborative Innovation Center on Forecast and Evaluation of Meteorological Disasters, Nanjing University
9 of Information Science and Technology, Nanjing 210044, China

10 ² State Key Laboratory of Severe Weather, Chinese Academy of Meteorological Sciences, Beijing 100081,
11 China

12 ³ National Meteorological Information Center, China Meteorological Administration, Beijing 100081, China

13 ⁴ Laboratory for Climate Studies of China Meteorological Administration, National Climate Center, Beijing
14 100081, China

15 ⁵ State Key Laboratory of Numerical Modeling for Atmospheric Sciences and Geophysical Fluid Dynamics,
16 Institute of Atmospheric Physics, Chinese Academy of Sciences, Beijing 100029, China

17 ⁶ Institute for Atmospheric and Climate Science, ETH Zurich, 8092 Zurich, Switzerland

18
19 *Corresponding to:* Hua Zhang (huazhang@cma.gov.cn)

20

21 **Abstract.** With high emissions of aerosols and the known world’s “Third Pole” of the Tibet Plateau (TP) in
22 East Asia, knowledge on the energy budget over this region is widely concerned. This study first attempts
23 to estimate the present-day land energy balance over East Asia by combining surface and satellite
24 observations, as well as the atmospheric reanalysis and Coupled Model Intercomparison Project phase 6
25 (CMIP6) simulations. Compared to the global land budget, a substantially larger fraction of atmospheric
26 shortwave radiation of 5.2% is reflected, highly associated with the higher aerosol loadings and more clouds
27 over East Asian land. While a slightly smaller fraction of atmospheric shortwave absorption of 0.6% is
28 unexpectedly estimated, possibly related to the lower water vapor content effects due to the thinner air over
29 the TP to overcompensate for the aerosol and cloud effects over East Asian land. The weaker greenhouse
30 effect and fewer low clouds due to the TP are very likely the causes for the smaller fraction of East Asian-
31 land surface downward longwave radiation. Hence, high aerosol loadings, clouds, and the TP over East Asia
32 play vital roles in the shortwave budgets, while the TP is responsible for the longwave budgets during this
33 regional energy budget assessment. The further obtained cloud radiative effects suggest that the presence of
34 clouds results in a larger cooling effect on the climate system over East Asian land than that over globe. This
35 study provides a perspective to help understand fully the roles of potential factors in influencing the
36 diversifying-different energy budget assessments over regions.

38 1. Introduction

39 Current patterns of Earth’s weather and climate are largely determined by the spatiotemporal
40 distributions of energy exchanges between the surface, atmosphere, and space. Theoretically, the outgoing
41 longwave radiation (OLR) is balanced by the incoming and reflected solar radiation at the top of the
42 atmosphere (TOA) to produce an equilibrium climate. The incoming solar radiation can be scattered by
43 clouds and aerosols or absorbed by the intermediary atmosphere, thereby contributing to the diverse energy
44 transformation at the surface (Trenberth et al., 2009; Wild et al., 2013a). The Earth’s surface energy balance
45 is of particular significance because it is the key driver of atmospheric and oceanic circulations, hydrological
46 cycles, and various surface processes (Wild et al., 2008; Mercado et al., 2009; Wild et al., 2013a; L’Ecuyer
47 et al., 2015). Anthropogenic influences on climate change are driven by the uneven distribution of the TOA
48 net radiation caused by forcings perturbed by variations of the atmospheric composition of greenhouse gases
49 and aerosols as well as aerosol-cloud interactions (Trenberth et al., 2009; Stephens et al., 2012; Wild et al.,
50 2013a; Trenberth et al., 2014; L’Ecuyer et al., 2015; Wild et al., 2019).

51 Many efforts have been made to quantify the magnitudes of different radiative components or energy
52 budgets in the climate system over a range of time-space scales, such as on global scales (Lin et al., 2008;
53 Trenberth et al., 2009; Stephens et al., 2012; Wild et al., 2013b; Wild et al., 2015; L’Ecuyer et al., 2015;
54 Wild et al., 2019; Wild, 2020), over land and ocean domains or the energy transport between them (Fasullo
55 and Trenberth, 2008a, b; Trenberth et al., 2009; Wild et al., 2015; L’Ecuyer et al., 2015), over the Arctic
56 (Previdi et al., 2015; Christensen et al., 2016), and over individual continents and ocean basins (L’Ecuyer
57 et al., 2015; Kim and Lee, 2018; Thomas et al., 2020). The energy balance at the TOA can be accurately

58 monitored by satellites from the most advanced Clouds and the Earth's Radiant Energy System (CERES)
59 Energy Balanced and Filled (EBAF) data product (Loeb et al., 2018), while considerably larger uncertainties
60 appear at the surface fluxes owing to weaker observational constraints (Raschke et al., 2016; Kato et al.,
61 2018; Huang et al., 2019). These assessments mostly build upon complementary approaches from a
62 combination of space and surface observations, climate models, and reanalyses. To date, the discrepancies
63 of independent global mean surface radiative fluxes have estimated to be within a few W m^{-2} (Wild, 2017a,
64 b), enabling the accurate quantification of global surface budgets. In addition, the surface radiative
65 components simulated by various climate models vary substantially in a range of around 10–20 W m^{-2} on
66 global scales, but exhibit greater inter-model discrepancies on regional scales (Li et al., 2013; Wild et al.,
67 2013a; Boeke and Taylor, 2016; Wild et al., 2015; Wild, 2017a, b, 2020). Existing challenges on the surface
68 energy estimates include considerable uncertainties from surface albedo and skin temperature, as well as the
69 partitioning of surface net radiation into sensible and latent heat (SH; LH) (Wild, 2017a, b).

70 Due to the large population and the largest emission source of aerosols and their precursors, East Asia,
71 especially China, has long been a hotspot in climate change research. Aerosols can interact with radiation
72 directly by scattering and absorbing solar/thermal radiation (Ghan et al., 2012) and indirectly by modifying
73 cloud microphysical properties and lifetimes (Li et al., 2011), thereby influencing Earth's radiation balance.

74 As the world's largest and highest plateau, the Tibet Plateau (TP) covers nearly one third of the East Asian
75 land area, significantly affecting the atmospheric circulation, energy budget, and water cycles of climate
76 system through its orographic and thermal effects (Liu et al., 2007; Xu et al., 2008a, b; Wu et al., 2015).
77 Deeper insights into the energy budget differences over East Asian and global land under the background of
78 high aerosol emissions and the role of the TP in East Asia are of the meaningful and essential attempts.

79 Moreover, clouds play a key role in modulating global and regional energy budgets and hydrological cycles
80 through increasing the reflected solar radiation and also the downward thermal radiation, leading to a cooling
81 and warming of climate system (Stephens, 2005; Wild et al., 2013a; Li et al., 2015; H. Wang et al., 2021).

82 Therefore, our emphasis in this study is on the regional characterization of the East Asian energy balance
83 under both all-sky and clear-sky conditions based on a combination of surface observations, satellite-derived
84 products, reanalysis, and Coupled Model Intercomparison Project phase 6 (CMIP6) models. The cloud
85 influence on the radiative energy budgets at the TOA, within the atmosphere, and at the surface is further
86 quantified over this region. Section 2 introduces the different data sources used in this study, including
87 surface and satellite observations, climate models, and reanalysis. Sections 3 and 4 provide detailed analyses
88 of the all-sky and clear-sky estimates of the energy balance components. The inferred cloud radiative effects
89 (CREs) at the TOA, within the atmosphere, and at the surface are presented in Section 5. Summary and
90 conclusions are given in Section 6. The present-day in this study represents years of 2010–2014, which
91 corresponds to the last five years of the historical simulations in CMIP6 climate models. East Asian land as
92 considered in this study consists of five countries, including China, Japan, South and North Korea, as well
93 as Mongolia.

94

95 2. Data sources

96 2.1. Surface observations

97 Considering the efforts to diminish the inhomogeneities in the measurement of ground-based surface
98 (downward) solar radiation (SSR) (Tang et al., 2011; Wang, 2014; Wang et al., 2015; Wang and Wild, 2016;
99 He et al., 2018; Yang et al., 2018, 2019) and the large amount of observational stations over China, the
100 homogenized monthly all-sky and clear-sky SSR datasets from the China Meteorological Administration
101 (CMA) National Meteorological Information Center (NMIC) are used in this study (<http://data.cma.cn/en/>)
102 (Yang et al., 2018, 2019). In this dataset, the clear-sky condition at observational sites is defined based on
103 the measured cloud fraction per day of no more than 15% (Yang et al., 2018). Taking clear-sky data (with
104 relatively complex missing months compared to the all-sky dataset) as an example, sites with more than one
105 year of > 2 missing months were deleted to ensure ≥ 4 years of available data during the period 2010-2014,
106 then the spline interpolation was performed on the missing months of the selected sites. As a consequence,
107 99 and 76 sites are available for the all-sky and clear-sky studies, respectively. Besides, to further explore
108 the [anthropogenic influence on SSR impacts from different site types](#), 84 (62) urban and 15 (14) rural stations
109 for all-sky (clear-sky) conditions are defined according to the administrative divisions of China (Wang et al.,
110 2017).

111 For the remaining East Asian sites, we use the monthly Global Energy Balance Archive (GEBA) dataset
112 (<http://www.geba.ethz.ch>) (Wild et al., 2017), which contains a worldwide widespread distribution of
113 monthly data from many sources, e.g., from the World Radiation Data Center (WRDC), the Baseline Surface
114 Radiation Network (BSRN), etc. Among these data sources, the BSRN dataset has a much higher precision
115 and temporal resolution (up to 1 min) compared to the GEBA, but its site number is very limited over East
116 Asia (only a few sites located in Japan and one site in Xianghe, China, but with no data available during this
117 study period), ~~thus making it impossible to obtain clear sky data using the clear sky detection algorithm.~~
118 Moreover, the relative random error of the monthly SSR from the GEBA data evaluated by Gilgen et al.
119 (1998) is 5%.

120 In order to retain as many sites as possible during the study period, we widen the selection criterion of
121 the GEBA data, i.e., sites with data ≥ 4 years and missing months ≤ 3 . Eventually, 8, 2, 4, and 14 sites are
122 selected from GEBA in China, Mongolia, South and North Korea, and Japan, respectively. Especially,
123 among the 14 sites in Japan, five pairs of the duplicate sites are obtained from the WRDC and BSRN sources,
124 respectively, and the left 4 sites are only from the WRDC (9 sites available). For China, only one site from
125 Hongkong out of 8 GEBA sites is not repetitive from the above-mentioned CMA sites (1 site available).
126 Therefore, 16 out of 28 GEBA sites are available under all-sky conditions (including 15 sites over regions
127 outside China and 1 site over Hongkong, China) by taking the average of these duplicate sites in Japan
128 instead, while the clear-sky reference sites are obtained from the interpolated CERES EBAF clear-sky
129 estimates at the GEBA sites (also 16 sites) due to the limited numbers of observational sites over these
130 regions. Additionally, we regard four island sites in Japan as rural stations (not shown in the figures), while
131 the sites in Mongolia as well as South and North Korea are all urban sites.

132 As shown in Fig. S1, there are 99 (rural/total: 15/99) and 16 (rural/total: 4/16) sites from the CMA and
133 GEBA available under all-sky conditions, respectively, whereas 76 (rural/total: 14/99) and 16 (from the
134 CERES-interpolated data at the 16 GEBA sites) sites are considered for clear-sky conditions, respectively.
135 More detailed station information is given in Table S1.

136

137 2.2. Satellite observation

138 Owing to the excellent temporal and spatial coverage of satellite instruments, CERES data products are
139 widely used to track variations of Earth's energy budgets. The newly released CERES EBAF Edition 4.1
140 with a monthly $1^\circ \times 1^\circ$ latitude-longitude resolution is used in this study (<https://ceres.larc.nasa.gov/data/>). In
141 this dataset, the TOA radiation components are adjusted within their uncertainty ranges based on the
142 independent observational ocean estimates of global heating rate (Loeb et al., 2018). Unlike the directly
143 measured TOA energy budget, the EBAF-surface energy fluxes are calculated by the cloud and aerosol
144 properties from satellite-derived products as well as the atmospheric profiles from reanalysis, with a lower
145 accuracy than their TOA counterparts (Kato et al., 2018). The uncertainty ranges in $1^\circ \times 1^\circ$ regional monthly
146 all-sky and clear-sky longwave (LW) and shortwave (SW) radiation fluxes at the TOA are also documented
147 by Loeb et al. (2018).

148

149 2.3. Climate models and reanalysis

150 Data from 40 CMIP6 climate models are used for the analyses in this study with their model
151 abbreviations, modeling groups, and resolutions in Table S2. A detailed description of the modeling groups
152 participating in CMIP6 is provided at <https://pcmdi.llnl.gov/CMIP6/>. The CMIP6 model-calculated radiation
153 fluxes under investigation for this study include energy budgets under both all-sky and clear-sky conditions
154 from 'historical all forcings' experiments covering the period 2010-2014. In these historical simulations,
155 both natural (e.g., solar variability and volcanic aerosols) and anthropogenic (e.g., greenhouse gases, aerosols,
156 and land use) forcings are considered to reproduce the climate change and evolution since preindustrial times
157 as accurately as possible (Eyring et al., 2016). Only the first ensemble member of each model is selected for
158 the analysis and the model numbers vary slightly among different available energy components.

159 In the long history of the European Center for Medium-range Weather Forecast (ECMWF), ERA5 is
160 the fifth generation product. It is a comprehensive reanalysis from 1979 (soon be backdated to 1950) to near
161 real time, which assimilates as many observations as possible in the upper air and near surface
162 (<https://cds.climate.copernicus.eu/>). Monthly means of the radiative components from ERA5 are used in this
163 study with a resolution of $0.25^\circ \times 0.25^\circ$ (regridDED to $1^\circ \times 1^\circ$). Compared to previous reanalyses (such as ERA-
164 Interim), a major strength of ERA5 is the much higher temporal and spatial resolutions, as well as a larger
165 number of vertical levels (Hersbach et al., 2020). Several independent studies have evaluated the
166 performance of ERA5 since its release. For example, excellent closure of the Arctic energy budget based on
167 ERA5 atmospheric data has been assessed by Mayer et al. (2019). The representation of surface irradiance

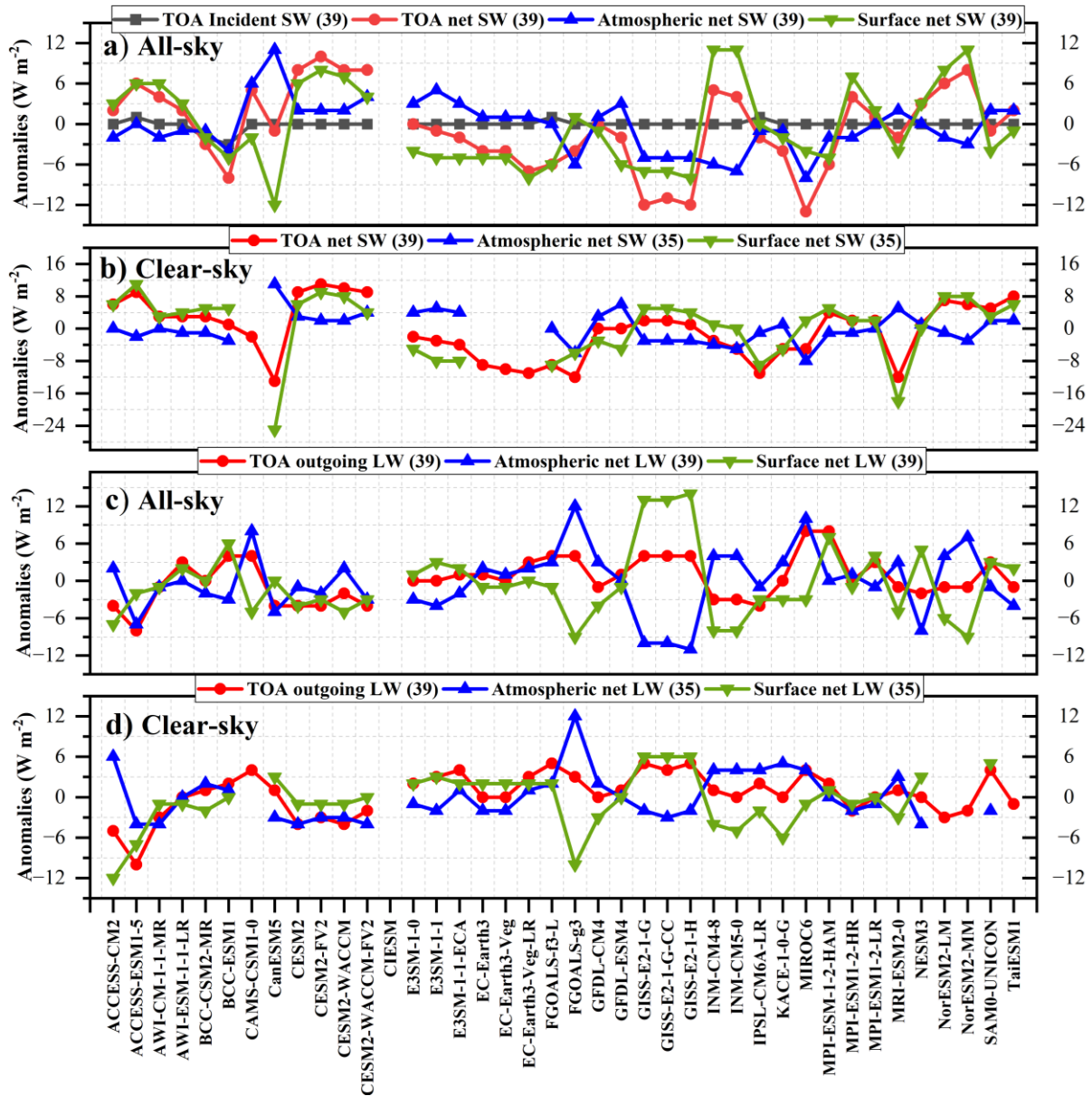
168 of ERA5 has been compared with other reanalyses and with ground and satellite observations (Trollet et al.,
 169 2018; Urraca et al., 2018). Specifically, Trollet et al. (2018) found that the surface solar irradiance over the
 170 tropical Atlantic Ocean from ERA5 exhibits fewer biases than the second version of the Modern-Era
 171 Retrospective Analysis for Research and Applications (MERRA-2). Urraca et al. (2018) reported that ERA5
 172 can be a valid alternative for satellite-derived products in terms of surface irradiance in most inland stations
 173 compared to ERA-Interim or MERRA-2.

174 **3. Assessment of land energy balance budgets under all-sky conditions**

175 3.1. Shortwave components

176 Under all-sky conditions, the present-day annual land-mean anomalies of TOA incident solar radiation
 177 as well as the SW net radiation at the TOA, within the atmosphere, and at the surface regarding to their
 178 respective multi-model means as simulated by various CMIP6 models over East Asia are shown in Fig. 1a.
 179 A summary of the CMIP6 model statistics (such as available model number, model spread, and the standard
 180 deviation (SD)), along with the corresponding multi-model mean, ERA5-, and CERES-derived estimates of
 181 different energy balance components are listed in Table 1. As shown in Fig. 1a, with the exception of the
 182 BCC-CSM2-MR and BCC-CESM1 models, all models give an estimate around 334 W m^{-2} for TOA
 183 incoming solar radiation with a very small SD of 0.2, closely matching the multi-model mean as well as the
 184 CERES and ERA5 estimates (Table 1). The multi-model means of solar absorption at the TOA, within the
 185 atmosphere, and at the surface are 217, 73, and 144 W m^{-2} , respectively, all within 2 W m^{-2} of the biases
 186 against the CERES-derived estimates, while they are 3–4 W m^{-2} larger for those from ERA5 at the TOA and
 187 within the atmosphere, yielding 1 W m^{-2} of bias against the CERES-based estimate at the surface (Table 1).
 188 However, the individual models vary significantly in their simulated annual East Asian land-mean solar
 189 absorption both at the TOA and surface (Fig. 1a), with SDs of around 6 W m^{-2} and inter-model spreads of
 190 more than 20 W m^{-2} (Table 1). Considering the smaller absolute amount of atmospheric and surface solar
 191 absorption compared to the TOA counterpart (73 and 144 vs. 217 W m^{-2} ; Table 1), the relative (percentage)
 192 differences relative to their respective multi-model means (relative (percentage) difference =
 193 $\frac{\text{range}}{\text{multi-model mean}} \times 100\%$) indicate that the uncertainties within the atmosphere and at the surface are larger
 194 than that at the TOA (i.e., TOA: $\frac{22}{217} \times 100\% = 10\%$; Atmosphere: $\frac{19}{73} \times 100\% = 26\%$; Surface:
 195 $\frac{23}{144} \times 100\% = 16\%$).

196



197

198 **Figure 1.** Annual land mean anomalies of (a, b) shortwave (SW) and (c, d) longwave (LW) budgets
 199 (Units: $W m^{-2}$) with regard to their respective multi-model means for present-day climate under (a, c)
 200 all-sky and (b, d) clear-sky conditions over East Asia as simulated by various CMIP6 models. The black, red,
 201 blue, and green lines represent the TOA incoming solar radiation, as well as the net SW/LW radiation at
 202 the TOA, within the atmosphere, and at the surface, respectively.

203

204 **Table 1.** Annual land mean estimates (Units: $W m^{-2}$) of the magnitudes of various energy balance
 205 components and cloud radiative effects (CREs) over East Asia under all-sky and clear-sky conditions at the
 206 TOA, within the atmosphere, and at the surface, respectively. The CMIP6 model statistics (e.g., available
 207 model number, spread, standard deviation (SD)), as well as the corresponding multi-model mean, ERA5-,
 208 and CERES-derived estimates are also given in the Table.

Component ($W m^{-2}$)	CMIP6				ERA5	CERES
	models	spread	SD	mean		
TOA						
Solar down	39	4	0.2	334	334	334
Solar up all-sky	39	23	6	-117	-115	-118

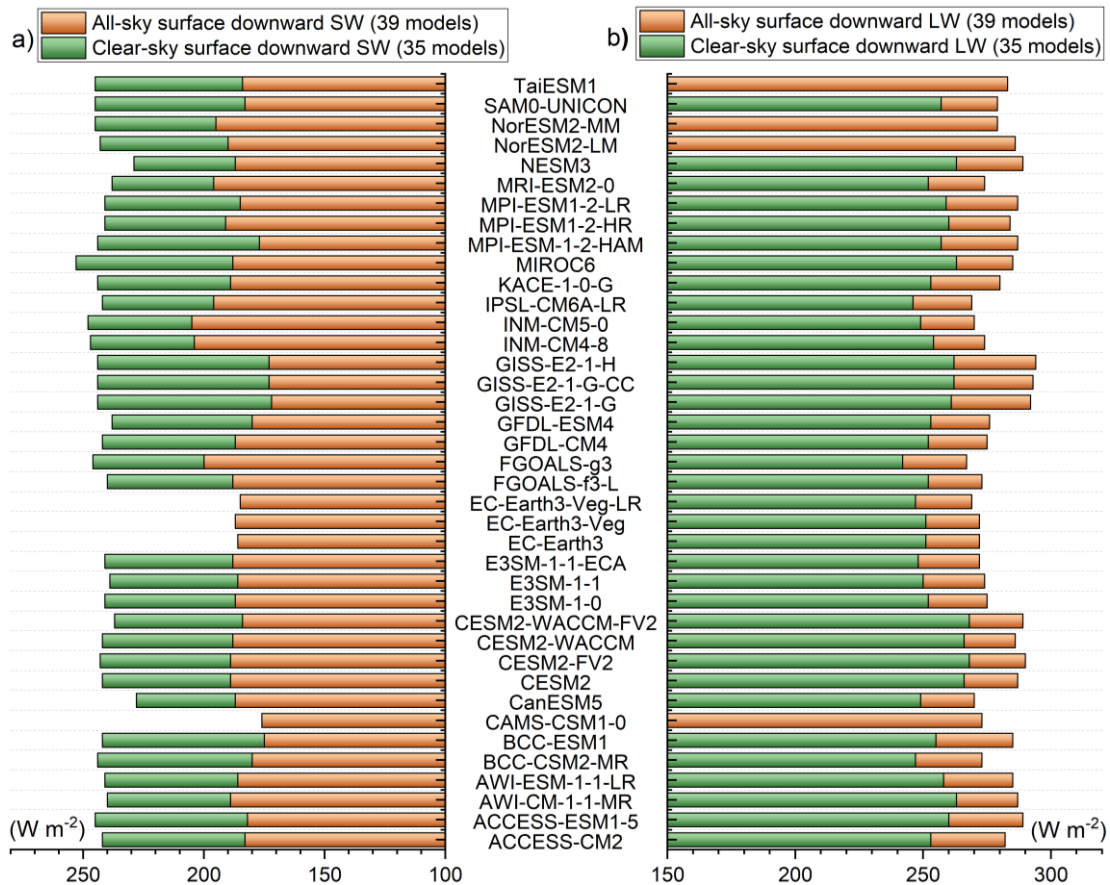
Solar net all-sky	39	22	6.1	217	219	216
Solar up clear-sky	39	24	7	-76	-78	-72
Solar net clear-sky	39	24	6.9	258	256	262
SW CRE	39	26	6.5	-41	-37	-46
Thermal up all-sky	39	12	3.5	-224	-225	-226
Thermal up clear-sky	39	15	3.2	-247	-246	-250
LW CRE	39	12	2.4	23	21	24
Net CRE	39	24	5.8	-18	-16	-22
Atmosphere						
SW absorption all-sky	39	19	3.8	73	78	74
SW absorption clear-sky	35	19	3.8	69	77	71
SW CRE	32	33	6.9	4	2	3
LW net all-sky	39	22	5.1	-152	-150	-157
LW net clear-sky	35	16	3.6	-151	-151	-154
LW CRE	32	14	3.3	-2	1	-3
Net CRE	32	35	7.8	1	2	0
Surface						
SW down all-sky	39	33	7.6	186	191	178
SW up all-sky	39	24	6.5	-43	-50	-36
SW absorbed all-sky	39	23	6.1	144	141	142
SW down clear-sky	35	25	4.6	242	238	236
SW up clear-sky	35	27	6.8	-53	-59	-45
SW absorbed clear-sky	32	36	7.8	189	179	191
SW CRE	35	28	6.6	-46	-38	-49
LW down all-sky	39	27	7.9	280	273	285
LW up all-sky	39	23	7.1	-352	-347	-354
LW net all-sky	39	23	5.7	-71	-74	-69
LW down clear-sky	35	26	6.8	256	253	256
LW up clear-sky	35	23	7.1	-351	-347	-353
LW net clear-sky	35	18	4.1	-95	-94	-97
LW CRE	35	12	3.5	24	20	27
net CRE	32	31	6	-21	-18	-22
net radiation	39	20	5.3	72	67	73
LH	40	26	4.7	-43	-38	—
SH	40	21	5.2	-31	-29	—

209

210 The simulated SSR, however, shows the largest spread of more than 30 W m⁻² (ranging from 172–205
211 W m⁻²) among all the substantially differing all-sky surface radiation components, with a large SD of 7.6 W
212 m⁻² (Fig. 2a; Table 1). The multi-model mean SSR is estimated to be 186 W m⁻², suggesting positive and
213 negative deviations of 8 and 5 W m⁻² from the CERES- and ERA5- derived estimates, respectively (Table
214 1). Interestingly, although the discrepancy between them is very large (8 or 5 W m⁻²), both the resulting
215 surface solar absorption differences are very small (within 3 W m⁻²), indicating that a higher SSR goes

216 together with a higher surface albedo (Table 1), which agrees well with that on a global mean level (Wild et
 217 al., 2015).

218



219

220 **Figure 2.** Annual land mean surface downward (a) SW and (b) LW radiation (Units: $W m^{-2}$) under both
 221 all-sky (orange bars) and clear-sky (green bars) conditions over East Asia as calculated by various CMIP6
 222 models.

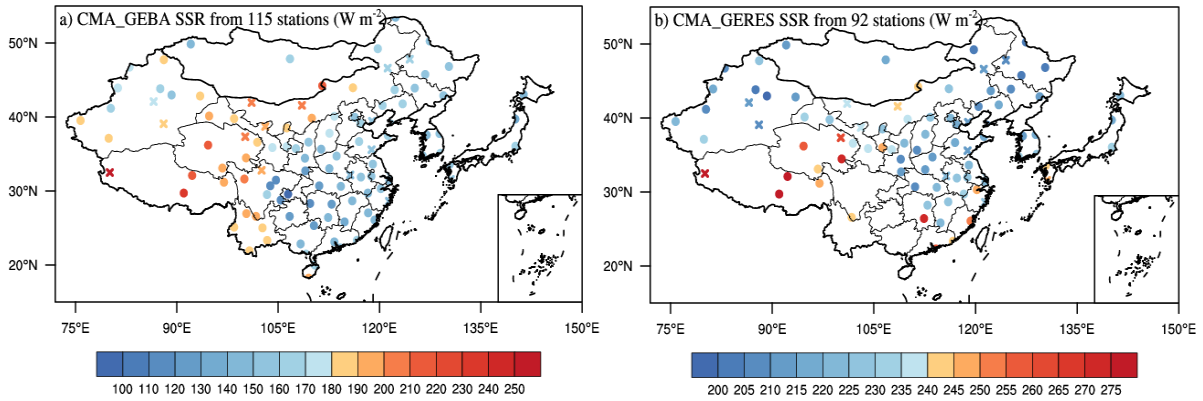
223

224 3.2. Best estimates for the surface downward SW radiation

225 As a major component of Earth's energy balance, the solar radiation reaching the Earth's surface
 226 governs a wide range of surface physical and chemical processes. The spatial distributions of the site-based
 227 annual mean SSR from the CMA and GEBA (Section 2.1) over East Asia under all-sky conditions are
 228 presented in Fig. 3a, together with the classified rural and urban sites. In short, the high values are mainly
 229 located at the high elevation stations over western China and a few island sites in Japan (e.g.,
 230 Minamitorishima, Japan; not shown in the figure), especially over the TP, with the largest value reaching
 231 $263 W m^{-2}$ (Geer, Tibet), which is associated with the high atmospheric transparency over these regions.
 232 However, the low annual mean values are primary over southwestern China, with the smallest value of 103
 233 $W m^{-2}$ (Shapingba, Chongqing), which is possibly caused by the higher aerosol loadings (Liao et al., 2015;

234 de Leeuw et al., 2018) and more clouds (Li et al., 2017; You et al., 2019; Lei et al., 2020; Zhang et al., 2020)
 235 over these regions. This distribution pattern is highly consistent with that over China documented by Q.
 236 Wang et al. (2021).

237



238

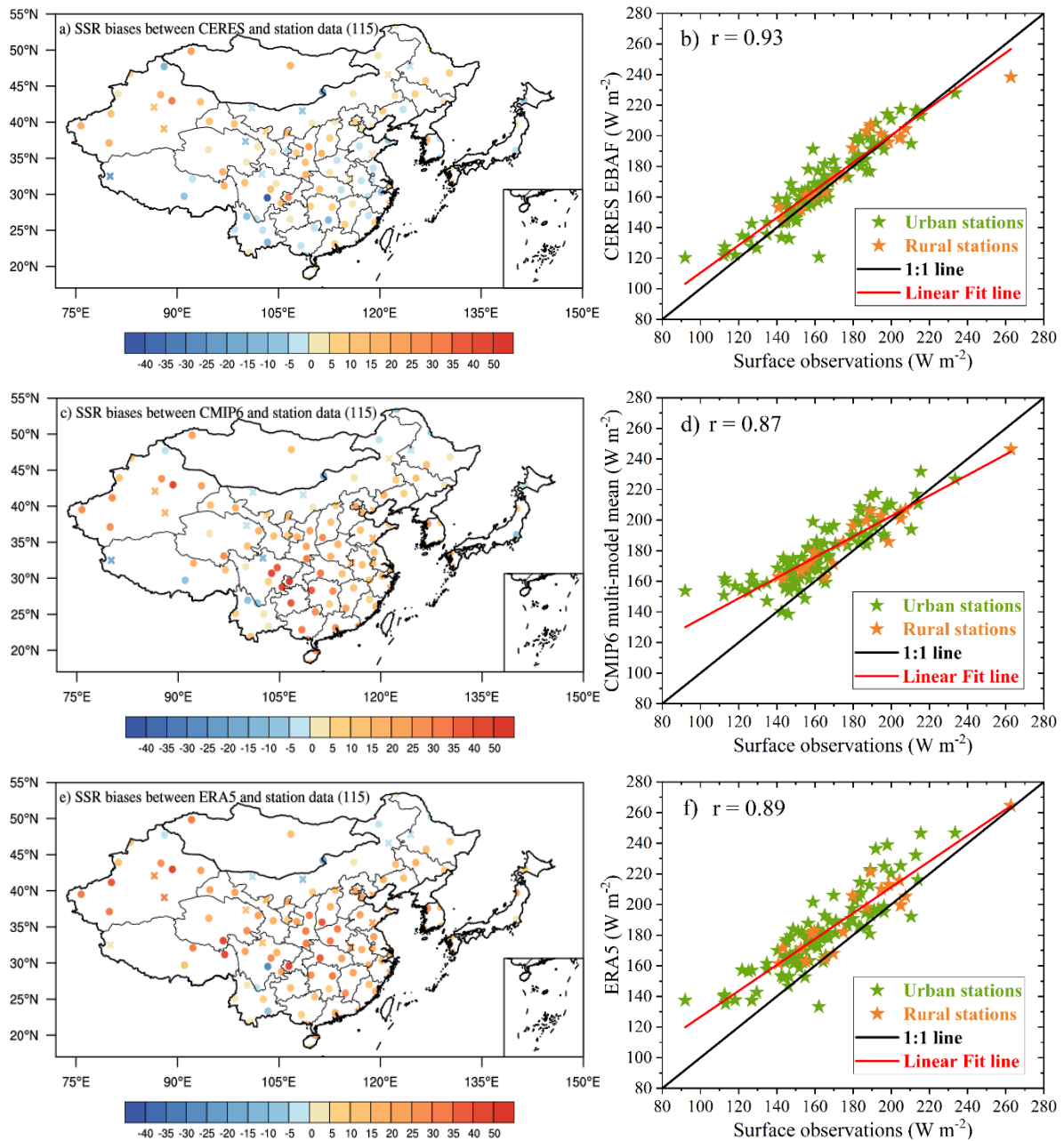
239 **Figure 3.** Spatial distributions of annual mean surface downward solar radiation (SSR) (Units: $W m^{-2}$) under
 240 (a) all-sky and (b) clear-sky conditions over East Asia. The all-sky sites are available from 99 CMA (China)
 241 and 16 GEBA (remaining regions outside China and one site in Hongkong, China) stations, while there are
 242 76 CMA and 16 CERES-interpolated sites for clear-sky conditions. The cross and circle symbols indicate
 243 rural (19 vs. 18 for all-sky and clear-sky conditions) and urban stations (96 vs. 74), respectively.

244

245 Figure 4 shows the distributions of annual mean SSR biases derived from the CERES, CMIP6 multi-
 246 model mean, and ERA5 against the surface observations, as well as the comparisons of their respective
 247 annual land means at the surface sites with their observed counterparts. The corresponding quantifications
 248 of the magnitudes of station-mean biases are also given in Table 2. According to the comparisons, they all
 249 correlate well with the ground-based observations, with their respective high correlation coefficients of 0.93,
 250 0.87, and 0.89, indicative of the highest accuracy in the CERES-derived estimate (Figs. 4b, d, and f). To
 251 quantify their SSR mean biases against the corresponding observed counterparts, the CERES-based bias at
 252 all sites is the smallest, with a station-mean bias of $3.8 W m^{-2}$, followed by the CMIP6 multi-model mean
 253 and the ERA5 reanalysis (with respective station-mean biases of 13.8 and $16.5 W m^{-2}$) (Table 2).
 254 Additionally, among all the aforementioned SSR estimates, the East Asian urban sites are in general more
 255 significantly overestimated than the rural sites on average compared to the surface observations (Figs. 4b, d,
 256 and f; Table 2). This further supports the argument that rural stations might be more representative for larger
 257 scale comparisons (e.g., the general circulation model grid scales) than the urban stations (which are
 258 vulnerable to local pollution) (Wang et al., 2018). The overestimations are mainly located in the high-latitude
 259 regions over East Asia for CERES-derived estimates (among them the underestimations mostly from rural
 260 sites), while the underestimates are primarily located in lower-latitude and eastern coastal regions (Figs. 4a
 261 and b). The CMIP6 multi-model mean and ERA5-derived SSR generally greatly overestimate the surface-
 262 based observations both at urban and rural sites, except for the regions over northern and northeastern Inner
 263 Mongolia, northwestern Heilongjiang (located in the northeastern China), and some individual sites over
 264 southwestern China (Figs. 4c-f). The annual land-mean area-weighted average SSR over East Asia derived

265 from CERES is estimated to be 178 W m^{-2} , which is closest to the surface observational estimate of 174 W m^{-2}
 266 m^{-2} , compared to the much higher overestimations of both the CMIP6 multi-model mean and ERA5 (186
 267 and 191 W m^{-2}) against the surface observations (Table 3), which shows a high consistency with their bias
 268 distributions and the collocated quantifications (Fig. 4; Table 2).

269



270

271 **Figure 4.** Spatial distributions of annual mean SSR biases (Units: W m^{-2}) derived from (a) CERES-EBAF,
 272 (c) CMIP6 multi-model mean, and (e) ERA5 reanalysis at a combination of the CMA and GEBA sites under
 273 all-sky conditions over East Asia. The corresponding comparisons of their respective annual means at the
 274 surface sites with their observed counterparts are displayed in (b), (d), and (f), respectively. The cross and
 275 circle symbols in Figs. a, c, e as well as the orange and green stars in Figs. b, d, f indicate rural and urban
 276 stations, respectively.

277

278 **Table 2.** Annual station-mean SSR biases (Units: $W m^{-2}$) derived from CERES-EBAF, CMIP6 multi-model
 279 mean, and ERA5 compared to the surface observational sites under all-sky and clear-sky conditions during
 280 2010-2014 over East Asian land, together with the separate station averages of biases ~~over~~at urban and rural
 281 sites. The largest percentages of SSR biases relative to their respective station-mean averages are estimated
 282 to be around 10% and 4% for all-sky and clear-sky conditions.

Station-mean SSR biases against surface sites (Units: $W m^{-2}$)	All-sky			Clear-sky		
	all	urban	rural	all	urban	rural
CERES-EBAF - surface sites	3.8	4.2	1.6	0.4	0.5	-0.3
CMIP6 - surface sites	13.8	15.0	7.4	9.1	9.7	6.4
ERA5 - surface sites	16.5	17.2	12.7	5.7	6.2	3.6

283

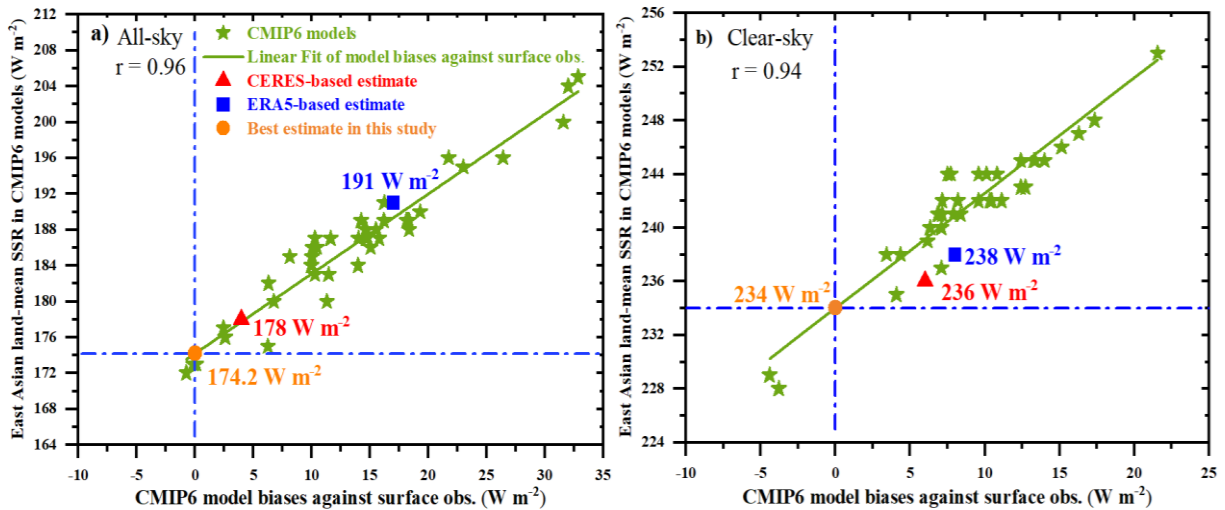
284 **Table 3.** Annual land mean area-weighted average SSR (Units: $W m^{-2}$) from a combination of the CMA and
 285 GEBA (CERES-interpolated) site observations under all-sky (clear-sky) conditions during the period 2010-
 286 2014 over East Asia, together with the corresponding estimates from the CERES-EBAF, CMIP6 multi-
 287 model means, and ERA5, respectively.

Average annual mean SSR during 2010-2014 over East Asia (Units: $W m^{-2}$)	Surface observations	CERES-EBAF	CMIP6	ERA5
All-sky	174	178	186	191
Clear-sky	230	236	242	238

288

289 However, the ground-based observations are spatially limited with sparse stations in some remote
 290 regions and are thus inadequate for many applications, as they may be not representative for real situations.
 291 To better constrain the large spread in the model-based SSR outlined above, we combine the ground-based
 292 observations to obtain the best estimate referring to the approach introduced in (Wild et al., 2013a). Figure
 293 5a gives various CMIP6 model biases of all-sky SSR at all the surface sites and their respective East Asian
 294 land means. The higher overestimations relative to surface observations generally correspond to higher
 295 model-based East Asian land means, with a much higher correlation coefficient of 0.96 than that of 0.88 on
 296 the global scale (Wild et al., 2015). Thus, the best estimate of the annual East Asian land-mean SSR is
 297 deduced to be $174.2 \pm 1.3 W m^{-2}$ (2σ uncertainty) in light of the linear regression analysis. The corresponding
 298 estimates from CERES and ERA5 are also labeled in the figure, at 178 and 191 $W m^{-2}$, respectively, implying
 299 a slight and substantial overestimation for CERES and ERA5 estimates. There is an overall tendency that
 300 most models overestimate the surface downward SW fluxes (36 out of 39 sites) compared to the ground-
 301 based observations, with a multi-model mean overestimation relative to site observations of $13.8 W m^{-2}$,
 302 which is also a longstanding issue in climate modelling (Wild et al., 1995; Wild et al., 2015).

303



304

305 **Figure 5.** Annual land mean SSR (Units: $W m^{-2}$) of various CMIP6 models as well as their respective model
 306 biases relative to an average over surface sites (99 CMA and 16 GEBA for all-sky; 76 CMA and 16 CERES-
 307 interpolated sites for clear-sky) under (a) all-sky and (b) clear-sky conditions during 2010-2014 over East
 308 Asia. Green stars represent various CMIP6 models. Best estimate here (orange circle) can be inferred from
 309 the intersection between the linear regression line (green solid lines) and the zero-bias line (blue dotted lines).
 310 Furthermore, the corresponding estimates from CERES-EBAF and ERA5 are also given by red triangle and
 311 blue square, respectively.

312

313 3.3. Longwave components

314 Similar to the all-sky SW counterparts, obvious discrepancies can still be noted in the annual land-mean
 315 LW radiation over East Asia among models, especially for those within the atmosphere and at the surface
 316 (Fig. 1c). Correspondingly, the simulated TOA OLR varies in a range of $12 W m^{-2}$, which is almost $10 W$
 317 m^{-2} lower than that within the atmosphere ($22 W m^{-2}$) and at the surface ($23 W m^{-2}$) (Table 1). The estimated
 318 annual East Asian land-mean TOA OLR from the CMIP6 multi-model mean is $-224 W m^{-2}$, within $2 W m^{-2}$
 319 of the deviations from the CERES- and ERA5-inferred estimates. The model spread of the simulated annual
 320 land-mean net LW radiation becomes larger from the TOA to the surface, with SDs of 3.5, 5.1, and $5.7 W$
 321 m^{-2} , respectively, which shows the same tendency as the relative (percentages) differences with respect to
 322 their multi-model means (5.4%, 14.5%, and 32.4%).

323 These large discrepancies in surface net LW radiation between models are particularly evident in the
 324 surface downward LW radiation (Fig. 2b; Table 1), with a range up to $27 W m^{-2}$ (from 267 to $294 W m^{-2}$)
 325 and a SD of $7.9 W m^{-2}$, which is also the largest deviation among all components under all-sky conditions.
 326 Compared to the CERES estimates, the slightly lower surface upward LW radiation (-352 vs. $-354 W m^{-2}$)
 327 and much lower surface downward LW radiation (280 vs. $285 W m^{-2}$) from the multi-model means are the
 328 major reason for the small deviation (within $2 W m^{-2}$) of the surface net LW radiation between them (Table
 329 1). It's interesting to note that the annual East Asian land-mean surface upward LW radiation estimated from
 330 the ERA5 is the lowest among all these estimates, at $-347 W m^{-2}$, suggesting the lowest surface skin
 331 temperature of the ERA5 product according to the Stefan-Boltzmann law, followed by the estimates from
 332 the multi-model mean and CERES (Table 1). In addition, the annual land-mean surface downward LW
 333 radiation estimated by ERA5 is $273 W m^{-2}$, approximately 7 and $12 W m^{-2}$ lower than the estimates by the

334 CMIP6 multi-model mean and CERES, respectively (Table 1). Therefore, both the lower surface upward
335 and downward LW radiation fluxes result in the small deviation in the estimated surface net LW radiation
336 from ERA5 compared to those from the multi-model mean and CERES (Table 1). Since the reanalysis
337 products take as many observed atmospheric parameters with global coverage as possible into consideration
338 during the radiative transfer calculations, they are widely used to obtain more accurate surface LW radiation
339 (Simmons et al., 2004; Wild et al., 2015). We also examined the corresponding surface LW fluxes from
340 another reanalysis, namely MERRA-2, and found much lower annual land means than those from ERA5, in
341 particular for the surface downward LW radiation (not shown), which arrives at the similar conclusions with
342 that documented by Urraca et al. (2018). Thus, considering the limited observational surface LW radiation
343 data over East Asia, ERA5 might be the best reference for the estimates of the annual land-mean surface
344 upward and downward LW radiation, at -347 and 273 W m^{-2} , respectively (Table 1).

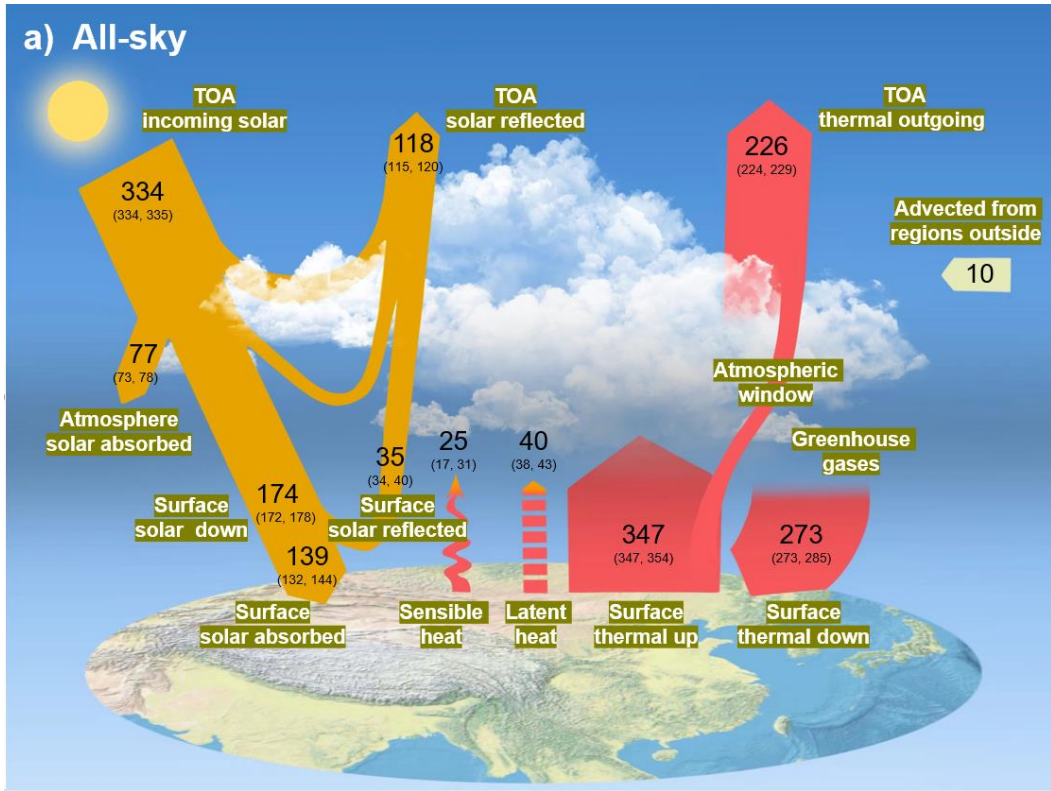
345

346 3.4. Discussion of land energy balance over East Asia under all-sky conditions

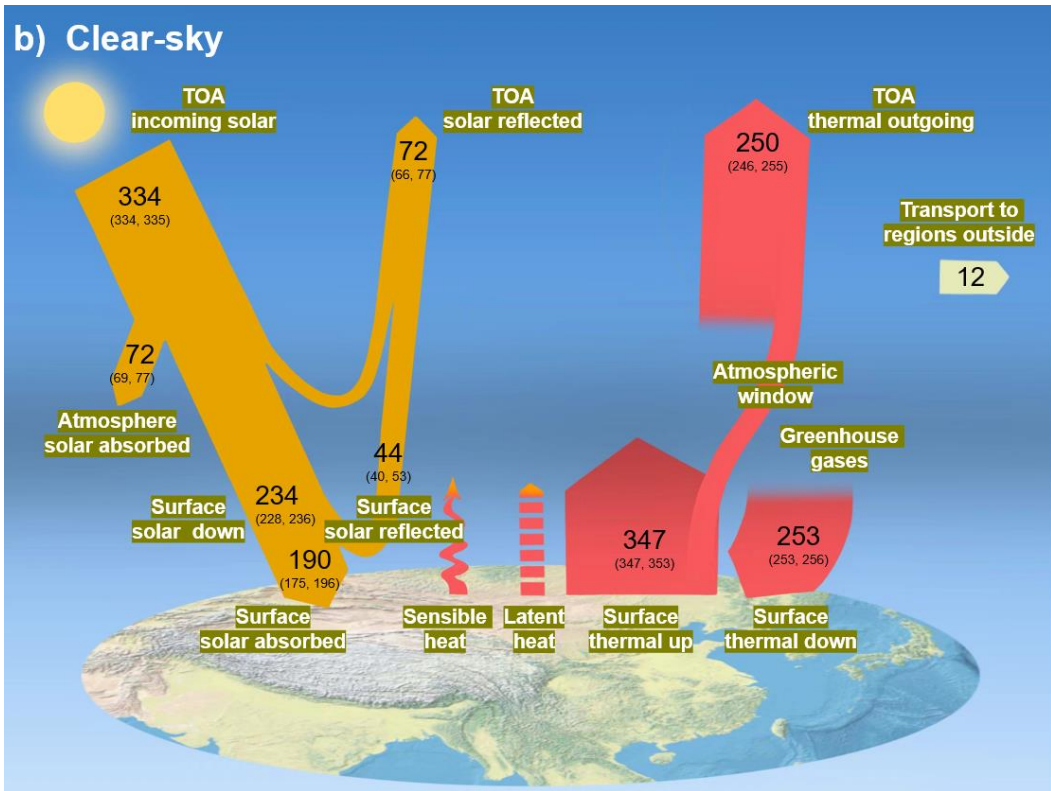
347 3.4.1. Radiative components

348 Figure 6a displays the schematic diagram of the all-sky land mean energy balance over East Asia,
349 including the above-mentioned SW and LW radiation budgets and other radiative components discussed in
350 the following. The estimated annual East Asian land-mean incoming, reflected, and net SW radiation as well
351 as the OLR at the TOA are therefore 334 , -118 , 216 , and -226 W m^{-2} (Table 1), respectively, based on the
352 CERES EBAF dataset. The corresponding uncertainties are obtained from the uncertainty of 2.5 (1σ
353 uncertainty) W m^{-2} for both SW and LW fluxes given by (Loeb et al., 2018). The annual East Asian land-
354 mean TOA OLR in CERES-EBAF is estimated to be 10 W m^{-2} larger than the TOA absorbed SW radiation,
355 implying an energy loss of 10 W m^{-2} at the TOA under all-sky conditions, which should be compensated by
356 the LH and SH transported from regions outside East Asia (Fig. 6a).

357



358



359

360 **Figure 6.** Diagrams of the annual land mean energy balance (Units: $W m^{-2}$) over East Asia under (a) all-
 361 sky and (b) clear-sky conditions for present-day climate. The uncertainty ranges are also given in
 362 parentheses.

363

364 For the SSR, the annual East Asian land-mean best estimate based on the CMIP6 multi-model
365 simulations and surface observations is 174.2 W m^{-2} (Fig. 5a and Fig. 6a). Considering the abnormally high
366 overestimation by ERA5 compared to surface observation, the high value of the uncertainty range is given
367 by the estimate from CERES EBAF (178 W m^{-2}), while its low value is from the lowest model estimate (172
368 W m^{-2} ; Fig. 2a) (Fig. 6a). The all-sky surface albedo information is derived from the ratio between the
369 CERES-derived surface upward and downward solar radiation, with a radiation weighted average of around
370 0.2 ($36.4/178.3$) over East Asian land. However, the corresponding surface albedos estimated by the CMIP6
371 multi-model mean and ERA5 are substantially higher than that from the CERES, with respective averages
372 of around 0.23 ($42.7/186.4$) and 0.26 ($49.6/191$). Considering the large spatial coverage of remote sensing
373 measurement to map albedo globally, the CERES-derived annual East Asian land-mean surface albedo is
374 adopted as the best estimate in this study. Therefore, considering the rounded best SSR estimate of 174 W
375 m^{-2} , the calculated surface reflected and absorbed SW radiation fluxes are around -35 and 139 W m^{-2} ,
376 respectively. As shown in Table 1, the uncertainty range of the surface absorbed SW radiation is 132 – 144
377 W m^{-2} according to the lowest value of CMIP6 models and the highest estimate among the aforementioned
378 estimates, which gives rise to an uncertainty range of the surface reflected solar radiation of 34 – 40 W m^{-2} .
379 Together with the annual East Asian land-mean SW absorption at the TOA and surface of 216 and 139 W
380 m^{-2} , the best estimate for the atmospheric SW absorption is therefore to be 77 W m^{-2} , which is within 4 W
381 m^{-2} of the differences between those estimated from the CMIP6 multi-model mean and CERES and closes
382 to the ERA5-derived estimate of 78 W m^{-2} (Table 1). The uncertainty range of the atmospheric SW
383 absorption is also determined by the estimates from different data sources as shown in Fig. 6a.

384 The downward LW radiation emitted by the atmosphere is mainly sensitive to the near-surface
385 temperature, water vapor, and cloud properties, while the surface emission is in proportion to the skin
386 temperature according to the Stefan-Boltzmann law. As analyzed in section 3.3, the best estimates of the
387 East Asian annual land-mean surface upward and downward LW radiation amount to -347 and 273 W m^{-2} ,
388 respectively, with uncertainty ranges coming also from the above-discussed different data sources (Fig. 6a).
389 The surface net LW radiation is then estimated to be -74 W m^{-2} based on the surface upward and downward
390 LW radiation outlined above. Combined with TOA outgoing thermal radiation of -226 W m^{-2} , the estimated
391 atmospheric net LW radiation is -152 W m^{-2} , which is close to the collocated estimates from the multi-model
392 mean (-152 W m^{-2}) and ERA5 (-150 W m^{-2}) but deviates substantially from the CERES-derived estimate of
393 -157 W m^{-2} (Table 1). Considering the surface absorbed SW radiation of 139 W m^{-2} , a best estimate for
394 surface net radiation is 65 W m^{-2} , suggesting that around 65 W m^{-2} of energy is available for the non-radiative
395 SH and LH. Besides, the ERA5 estimate of 67 W m^{-2} is very close to the best estimate of 65 W m^{-2} , while
396 much higher estimates of 72 and 73 W m^{-2} are obtained from the multi-model mean and CERES (Table 1),
397 respectively.

398

399 3.4.2. Nonradiative components

400 The surface net radiation is mainly balanced by the non-radiative components of SH and LH in addition
401 to a very small proportion of ground heat flux and melt (less than 1%) (Ohmura, 2004). However, due to the
402 lack of constraints from in-situ and space observations, this partitioning of the surface net radiation into SH
403 and LH is still subject to considerable uncertainties. As shown in Fig. S2, the simulated annual East Asian
404 land-mean LH and SH vary greatly between different models, with a range of 26 and 21 W m⁻², respectively,
405 as well as the relative discrepancies relative to their respective multi-model means of 60% ($\frac{26}{43} \times 100\%$) and
406 68% ($\frac{21}{31} \times 100\%$), respectively, showing larger discrepancies between models with larger uncertainties in SH
407 (Table 1). The best SH estimate can therefore be obtained from the residual of the LH. To obtain a more
408 accurate surface LH from available datasets of the multi-model mean and ERA5, we take an average of them
409 as the best estimate, namely -40 W m⁻², the uncertainty ranges of which are also given according to these
410 estimates (Fig. 6a). Note that all the values in this study are calculated on the basis of one decimal point,
411 which may result in 1 W m⁻² of bias during the rounding process. Combined with the surface net radiation
412 and LH of 65 and -40 W m⁻², respectively, the surface SH is estimated to be -25 W m⁻², the uncertainty range
413 of which is also given by the existing estimates from various CMIP6 models and ERA5 (Fig. 6a). In addition,
414 although the annual land-mean SH estimated from the MERRA-2 is much higher than the estimates from
415 multi-model mean and ERA5 (not shown), the estimated LH is around -39 W m⁻² (not shown), very close to
416 the best estimate of -40 W m⁻², which increases our confidence in the estimation of this quantity.

417

418 3.4.3. Comparisons with global annual land-mean estimates

419 Notable discrepancies exist in the global land-mean energy budgets reported by Wild et al. (2015) and
420 the regional land-mean estimates over East Asia in this study (Fig. S3; Table 4). For the SW budgets, the
421 estimated annual land-mean TOA incident solar radiation over East Asia is 9 W m⁻² higher than that over
422 global land (334 vs. 325 W m⁻²), implying a slightly lower land-mean solar zenith angle over East Asia.
423 Comparisons also show a slightly higher relative percentage of TOA reflected solar radiation of 0.8% despite
424 of the much lower surface reflected SW radiation of 4.3% over East Asian land compared to global land with
425 respect to their respective TOA incident solar radiation (thereafter call ‘relative percentage’ for short). This
426 suggests much more relative atmospheric SW reflection of 5.2% over East Asian land, which agrees fairly
427 well with more aerosols (Wei et al., 2019) and clouds (King et al., 2013; Fan et al., 2018; also see Fig. S4)
428 over this region compared to global land. However, the annual land-mean solar radiation reaching the East
429 Asian surface is around 10 W m⁻² lower than that over global land (174 vs. 184 W m⁻²), approximately
430 accounting for 52.1% and 56.6% of their respective incident solar radiation at the TOA, respectively,
431 indicating lower fraction of solar energy arriving at the East Asian surface compared to global land. Together
432 with the lower annual land-mean surface albedo over East Asian land compared to global land (20% vs.
433 26%), this leads to the similar relative percentages of surface absorptions (41.6% vs. 41.9%). Although the
434 magnitude of the atmospheric SW absorptions over East Asian and global land are nearly the same (both
435 around 77 W m⁻²), the corresponding relative percentage over East Asian land is a little bit lower than that

436 over global land (around 0.6%). This is somewhat unexpected due to the fact of more clouds and aerosol
 437 loadings over East Asian land, which is possibly offset by the lower water vapor contents caused by the
 438 higher altitudes and thinner air over the TP.

439

440 **Table 4.** Comparisons of the annual mean SW/LW energy balance components (Units: $W\ m^{-2}$) over East
 441 Asian land (this study) and global land (Wild et al., 2015) as well as the corresponding relative percentages
 442 with regard to their respective TOA incident solar radiation/surface LW emissions, along with the relative
 443 percentage differences between them.

Component	East Asian land		Global land		Percentage difference
	Annual mean	Relative percentage	Annual mean	Relative percentage	
SW budget					
TOA solar down	334	1	325	1	—
TOA solar up	-118	35.3%	-112	34.5%	0.8%
Atmospheric SW absorption	77	23.1%	77	23.7%	-0.6%
Atmospheric SW reflection	-83	24.9%	-64	19.7%	5.2%
Surface solar down	174	52.1%	184	56.6%	-4.5%
Surface solar up	-35	10.5%	-48	14.8%	-4.3%
Surface solar absorption	139	41.6%	136	41.9%	-0.3%
LW budget					
TOA LW up	-226	65.1%	-232	62.4%	2.7%
Atmospheric LW absorption	-152	43.8%	-166	44.6%	-0.8%
surface LW down	273	78.7%	306	82.3%	-3.6%
Surface LW up	-347	1	-372	1	—

444

445 For the LW budgets, the regional surface LW emission over East Asia is estimated to be much lower
 446 than the global land-mean estimates in Wild et al. (2015) (Fig. S3), which mainly results from the lower
 447 temperature over the TP induced by high altitudes. The relative percentage of land mean surface downward
 448 LW radiation with respect to the surface emission over East Asia is about 78.7 %, which is lower than the
 449 global estimate of 82.3%, corresponding well to a reduction in greenhouse effect and fewer low clouds due
 450 to the TP (Fig. S4) considering its coverage over East Asian land. Ultimately, a higher percentage of LW
 451 radiation is emitted to space over East Asian land compared to global land (65.1% vs. 62.4%). Our estimates
 452 also indicate approximately similar amounts of LH (40 vs. 38 $W\ m^{-2}$) and much lower SH (25 vs. 32 $W\ m^{-2}$)
 453 over East Asia compared to the global land-mean estimates (Fig. S3), which is possibly related to the
 454 lower East Asian-land surface temperature.

455 In general, as can be concluded from Table 4, although much less surface SW radiation of 4.3% is
 456 reflected over East Asian land compared to global land, a slightly more SW reflection of 0.8% is estimated
 457 at the TOA, indicating much larger atmospheric SW reflection of 5.2% due to the stronger scattering from
 458 aerosols and clouds over East Asian land than global land. However, the SW absorption within the
 459 atmosphere over East Asian land is 0.6% lower than that over global land despite of the more absorption
 460 from clouds and aerosols, which is possibly offset by the lower water vapor contents caused by the thinner
 461 air over the TP. The lower surface temperature, weaker greenhouse effect and fewer low clouds due to the
 462 high altitudes and the thinner air over the TP in East Asian land are the major reasons for the relative lower

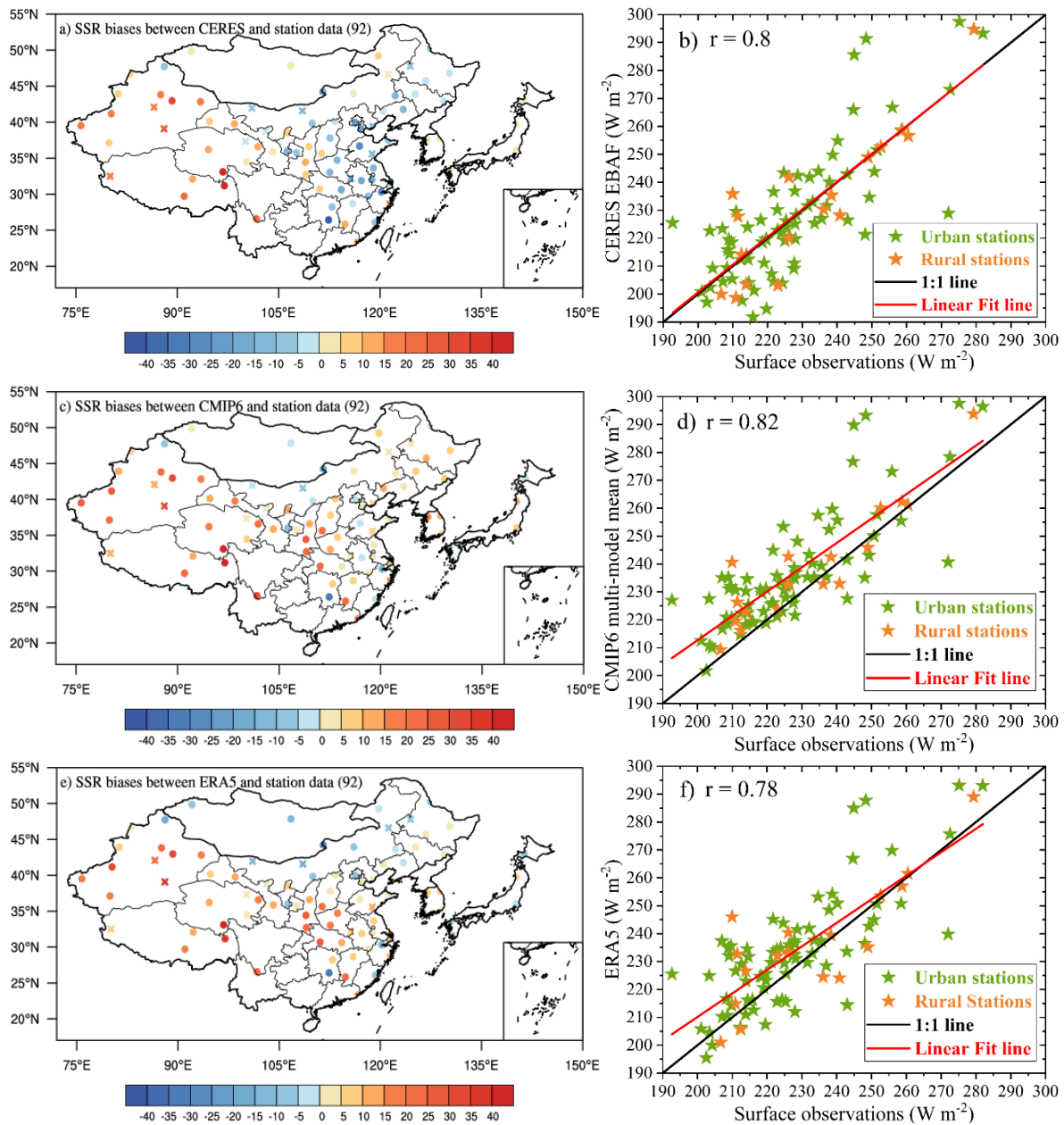
463 surface LW emission, less and more fractions of surface downward LW radiation of 3.6% and the OLR of
464 2.7% over East Asian land compared to global land, respectively.

465

466 **4. Assessment of land energy balance budgets under clear-sky conditions**

467 The clear-sky land energy balance budgets over East Asia are similarly evaluated as all-sky conditions.
468 Detailed analyses are given in Supplemental material if interested. The annual land-mean SW clear-sky
469 absorptions at the TOA and surface over East Asia show larger variations among different models than that
470 under all-sky conditions (Fig. 1a and b; Table 1), which is consistent with that reported by Wild et al. (2019)
471 but is amazingly in contrast to the recognition that the representation of clouds is the largest uncertainties in
472 climate models (Dolinar et al., 2015). Specially, the surface SW clear-sky absorptions simulated by various
473 models still exhibit a larger uncertainty than the TOA counterparts despite of the lower absolute values (Fig.
474 1b; Table 1). Contrary to the all-sky counterparts, the simulated clear-sky SSR among different models,
475 shows notably smaller inter-model spread and SD than the surface SW absorptions (Table 1), with much
476 smaller model discrepancy compared to the all-sky conditions (Fig. 2a; Table 1).

477 To further constrain the outlined inter-model discrepancy of the simulated clear-sky SSR, surface
478 observations from the CMA and CERES-interpolated estimates at the GEBA sites are utilized in this study.
479 The high values of the station-based clear-sky SSR are mainly located in the TP, but with an abnormally
480 high value located at the southern China (Fig. 3b). All the East Asian land-mean clear-sky SSR estimates
481 from CERES, CMIP6 multi-model mean, and ERA5 agree reasonably well with the surface observations,
482 but with smaller correlation coefficients ranging from 0.78 to 0.82 compared to the all-sky conditions (Figs.
483 7 b, d, and f). The CERES-derived clear-sky SSR is mainly overestimated in central and western China, but
484 with slight underestimations mainly located in northeastern, eastern, and southern China (Fig. 7a). Similar
485 bias patterns can also be found in the clear-sky SSR from the CMIP6 multi-model mean and ERA5 compared
486 to the surface observations, except for some individual sites over northeastern Inner Mongolia, eastern China,
487 western Mongolia, and Japan (Figs. 7c and e), but with relatively smaller overestimations than the all-sky
488 counterparts (Figs. 4c and e; Table 2). Specifically, the smallest station mean bias in CERES-derived SSR
489 compared to the multi-model mean and ERA5 (Table 2) can be attributed to its even distributed surface sites
490 of overestimations and underestimations (Figs. 7b, d, f). Again, among all the aforementioned clear-sky SSR
491 biases, more overestimations exist in urban stations than the rural stations (b, d, f in Figs. 4 and 7; Table 2).
492 Consequently, all East Asian land-mean area-weighted averages of clear-sky SSR from CERES, CMIP6
493 multi-model mean, and ERA5 show higher overestimations of around 6, 12, and 8 W m^{-2} , respectively,
494 compared to the surface observed counterpart of 230 W m^{-2} (Table 3). Based on the similar method
495 introduced in Wild et al. (2015), the best estimate for the East Asian land-mean clear-sky SSR is determined
496 to be $234 \pm 1.1 \text{ W m}^{-2}$ (2σ uncertainty), with a slightly smaller correlation coefficient of 0.94 and smaller
497 deviations from the CERES and ERA5 estimates compared to the all-sky counterparts (Fig. 5b; Table 3).
498 Besides, the overestimations still exist in the observed land-mean clear-sky SSR for most climate models
499 over East Asia, with a smaller multi-model mean overestimation of 9.1 W m^{-2} than the all-sky counterparts.



501

502 **Figure 7.** Spatial distributions of annual mean SSR biases derived from (a) CERES-EBAF, (b) CMIP6
 503 multi-model mean, and (c) ERA5 reanalysis against surface observations from a combination of the CMA
 504 and CERES-interpolated sites under clear-sky conditions over East Asia. The corresponding comparisons of
 505 their respective annual land means at the surface sites with their observed counterparts are displayed in (b),
 506 (d), and (f), respectively. The cross and circle symbols in Figs. a, c, e as well as the orange and green stars
 507 in Figs. b, d, f indicate rural and urban stations, respectively.

508

509 This clear-sky energy budget only represents the removal of cloud but maintains the same atmospheric
 510 conditions as the all-sky conditions, which is not balanced because it is not the equilibrium state the Earth
 511 would achieve when no clouds could form. Ultimately, the clear-sky East Asian land-mean energy budget is
 512 not closed and with no quantifications of SH and LH established—as displayed in Fig. 6b. In addition to the
 513 analyses above, the clear-sky TOA energy budgets are derived from CERES-derived product, with

514 uncertainty ranges referred to Loeb et al. (2018), while the surface LW budgets are again from ERA5
 515 reanalysis. Also, additional clear-sky radiation weighted surface albedo of 0.19 from CERES is obtained to
 516 estimate the surface reflected and absorbed SW radiation. All the uncertainty ranges are given by different
 517 data sources from various CMIP6 models, as well as the multi-model mean, CERES-, and ERA5-derived
 518 estimates, except for their TOA counterparts.

519 We doublecheck the energy balance components evaluated in this study by referring to the uncertainty
 520 ranges from CERES-derived product given by Kato et al. (2018) (Table 5), which indicates that all estimated
 521 energy components fall within these uncertainty ranges, except for the all-sky surface downward LW
 522 radiation, with about 3 W m^{-2} lower than the corresponding lowest CERES range. This is in line with its
 523 much higher CERES-derived estimate compared to that of the ERA5 (285 vs. 273 W m^{-2}) (Table 1).

524

525 **Table 5.** Uncertainties (Units: W m^{-2}) in $1^\circ \times 1^\circ$ regional monthly surface SW, LW, and net (SW + LW)
 526 fluxes under all-sky and clear-sky conditions for the CERES-EBAF Edition 4.1 product (referring to Kato
 527 et al. (2018)), as well as its corresponding estimates of various surface fluxes.

Uncertainties(1σ)	All-sky	Clear-sky
SW down	178 ± 14	236 ± 6
SW up	36 ± 11	45 ± 11
SW net	142 ± 13	191 ± 13
LW down	285 ± 9	256 ± 8
LW up	354 ± 15	353 ± 15
LW net	69 ± 17	97 ± 17
SW + LW net	73 ± 20	95 ± 20

528

529 Overall, around 21.6% and 56.9% of the TOA incoming solar radiation are absorbed by the atmosphere
 530 and surface, respectively, for clear-sky conditions, while these absorptions are 23.1% and 41.6% for all-sky
 531 conditions. This implies that the existence of clouds results in more atmospheric SW absorption of around
 532 1.5% and much less surface solar absorption of around 15.3% with respect to the TOA incoming solar
 533 radiation.

534

535 **5. The cloud radiative effects (CREs)**

536 According to the annual land-mean best estimates of radiative components over East Asia under all-sky
 537 and clear-sky conditions obtained in previous sections, the present-day CREs can be inferred quantitatively
 538 over this region. The calculated SW, LW, and net CREs at the TOA, within the atmosphere, and at the
 539 surface are therefore presented in Fig. 8. Moreover, the corresponding calculation formulas are also given in
 540 the followings:

541

$$542 \text{ TOA SW CRE} = \text{TOA outgoing SW}_{\text{all-sky}} - \text{TOA outgoing SW}_{\text{clear-sky}}$$

543 $TOA\ LW\ CRE = TOA\ outgoing\ LW_{all-sky} - TOA\ outgoing\ LW_{clear-sky}$

544 $TOA\ Net\ CRE = TOA\ SW\ CRE + TOA\ LW\ CRE$

545

546 $Surface\ Net\ SW\ CRE = Surface\ Net\ SW_{all-sky} - Surface\ Net\ SW_{clear-sky}$

547 $Surface\ Net\ LW\ CRE = Surface\ Net\ LW_{all-sky} - Surface\ Net\ LW_{clear-sky}$

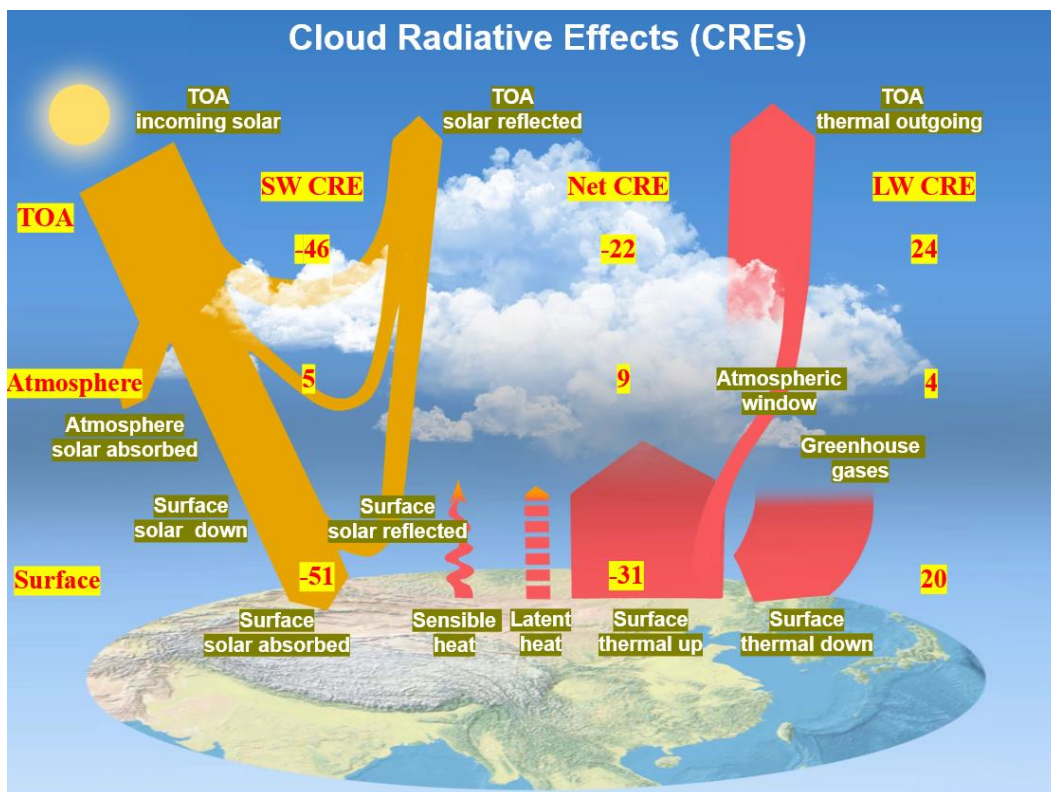
548 $Surface\ Net\ total\ CRE = Surface\ Net\ SW\ CRE + Surface\ Net\ LW\ CRE$

549

550 $Atmospheric\ SW\ CRE = TOA\ SW\ CRE - Surface\ Net\ SW\ CRE$

551 $Atmospheric\ LW\ CRE = TOA\ LW\ CRE - Surface\ Net\ LW\ CRE$

552



553

554 **Figure 8.** Diagram of the annual land mean SW, LW, and net (SW + LW) cloud radiative effects (CREs)
 555 (Units: $W\ m^{-2}$) at the TOA, within the atmosphere, and at the surface over East Asia, calculated by the
 556 differences between all-sky and clear-sky radiation budgets as given in Fig. 7.

557

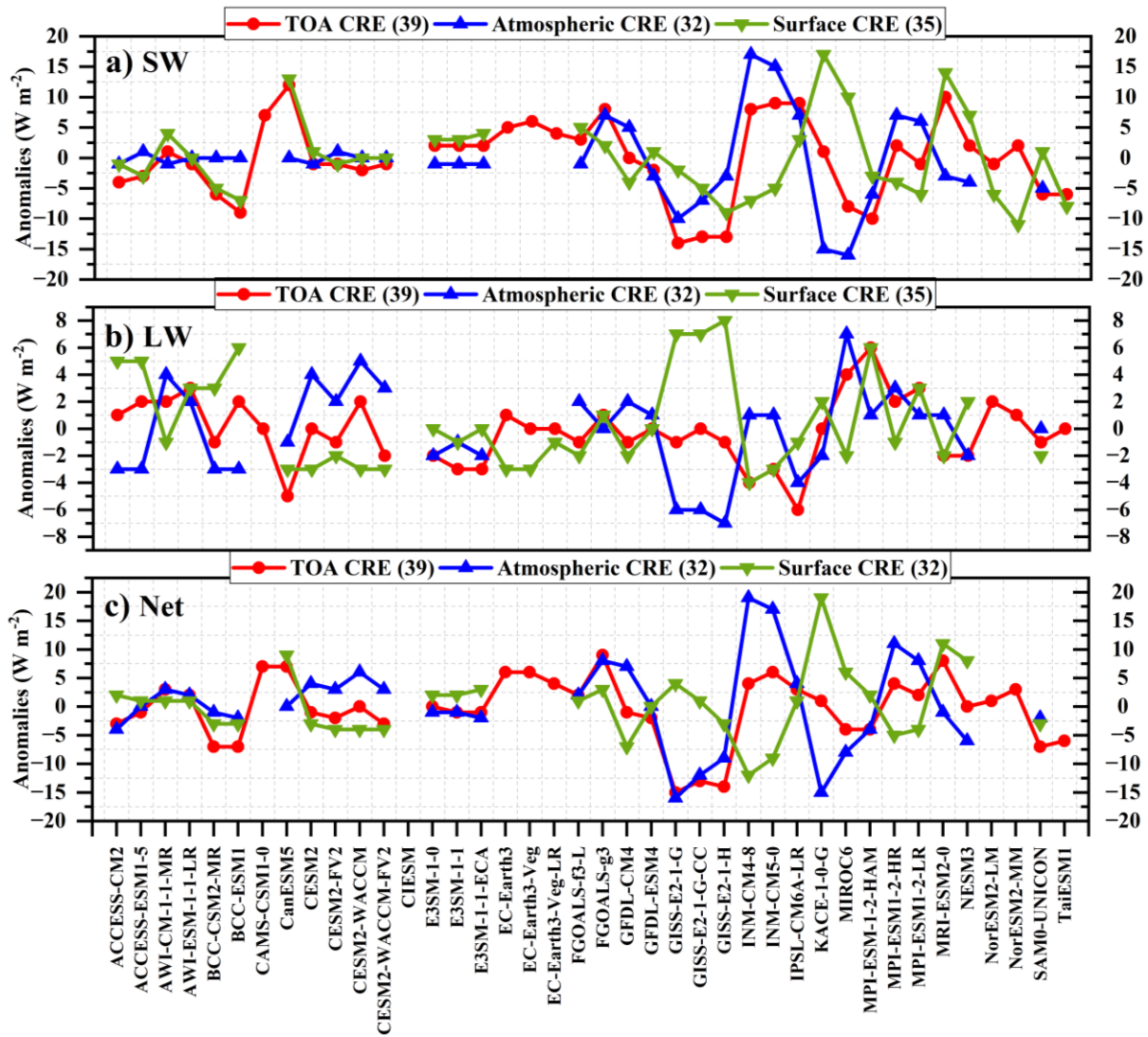
558 Best estimates for the annual East Asian land-mean reflected solar radiation at the TOA under all-sky
 559 and clear-sky conditions are -118 and $-72\ W\ m^{-2}$, respectively, differing by $-46\ W\ m^{-2}$, indicating that the
 560 clouds give rise to an extra $46\ W\ m^{-2}$ solar reflection at the TOA, thus cooling the Earth-atmosphere system.

561 Similarly, the TOA LW CRE, obtained as the difference between the TOA thermal radiation under all-sky
562 and clear-sky conditions, is 24 W m^{-2} , suggesting a warming effect of clouds on the system. Thus, the
563 estimated TOA net CRE is -22 W m^{-2} , pointing out that the overall effects of clouds result in an energy loss
564 and net cooling to the system, not only in the global mean, but also over East Asian land.

565 At the Earth's surface, the shading effects of clouds are estimated to reduce the surface solar radiation
566 by 60 W m^{-2} , from 234 to 174 W m^{-2} , while the surface solar absorption differs by 51 W m^{-2} , from 190 to
567 139 W m^{-2} , namely the surface net SW CRE is -51 W m^{-2} . On cloudy skies, the estimated surface downward
568 LW radiation increases from 253 to 273 W m^{-2} , with an increase of 20 W m^{-2} , illustrating that the surface
569 net LW CRE is 20 W m^{-2} and therefore leads to a surface warming. Thus, the surface net CRE, i.e., the sum
570 of the surface net SW and LW CRE, is then -31 W m^{-2} , indicating that clouds contribute more to the SW
571 energy budgets. Eventually, the clouds lead to the enhancement of the SW and LW absorption within the
572 atmosphere of around 5 and 4 W m^{-2} , respectively, thus resulting in an atmospheric net CRE of 9 W m^{-2} over
573 East Asian land.

574 The above CRE estimates are compared to the corresponding estimates from different data sources (Fig.
575 9; Table 1). Generally, compared to the LW CREs (Fig. 9b), the simulated SW CREs show larger spreads
576 and SDs amongst models (Fig. 9a; Table 1). For the SW CREs at the TOA, within the atmosphere, and at
577 the surface, the CERES-derived estimates match perfectly with the best estimates mentioned above, within
578 2 W m^{-2} of the biases, followed by the estimates from the multi-model means and ERA5 (Table 1). For the
579 LW CREs, the calculated TOA LW CREs from the CMIP6 multi-model mean and CERES differ by no more
580 than 1 W m^{-2} compared to the best estimate, while large differences are noted at the surface LW CREs,
581 thereby leading to their opposite signs in the atmospheric LW CREs (Fig. 9b; Table 1). Specifically, since
582 the ERA5-based TOA LW CRE deviates by no more than 3 W m^{-2} with the best estimate of 24 W m^{-2} with
583 nearly the same surface LW CRE, the estimated atmospheric LW CRE is therefore the closest to the best
584 estimate (Table 1). This is owing to the fact that we make use of the ERA5 data as the reference to estimate
585 the surface LW radiation. Thus, the major reason for the large discrepancies in the atmospheric and surface
586 LW CREs estimated from different data sources with respect to the best estimates in this study is the
587 determination of the surface downward and upward LW radiation, which is also the reason for the large
588 deviations in their net CREs (Fig. 9c).

589



590

591 **Figure 9.** Annual land mean anomalies of (a) SW, (b) LW, and (c) net (SW + LW) CRE (Units: W m⁻²) at
 592 the TOA (red line), within the atmosphere (blue line), and at the surface (green line) with regard to their
 593 respective multi-model means over East Asia, respectively, as represented by various CMIP6 models. The
 594 numbers in the parentheses indicate the available CMIP6 climate models for the corresponding radiation
 595 components.

596

597 A better comparison with the global annual mean best estimates of CREs by Wild et al. (2019) is given
 598 in Fig. S5. At the TOA, a slightly lower and much lower East Asian land-mean SW and LW CREs of 1 W
 599 m⁻² and 4 W m⁻² result in 3 W m⁻² more energy loss at the TOA compared to the globe. At the surface, much
 600 lower annual East Asian land-mean SW and LW CREs by 3 W m⁻² and 8 W m⁻² are estimated compared to
 601 the values over the globe, leading to a net CRE deviation of 5 W m⁻², indicative of 5 W m⁻² more energy loss
 602 at the surface. However, lower and higher annual East Asian land-mean SW and LW CREs of 2 and 4 W m⁻²
 603 within the atmosphere contribute to the nearly close net CRE with a deviation of no more than 2 W m⁻²
 604 compared to the global mean estimates. On the whole, lower annual East Asian land-mean best estimates in
 605 the absolute values of surface SW and LW CREs as well as the TOA LW CRE compared to their global
 606 mean counterparts give rise to the CRE differences between them.

607 6. Summary and conclusions

608 This study aims to explore how the energy budgets are interrupted by the complex orographic and
609 thermal effects of the TP, as well as the high anthropogenic aerosol emissions over East Asian land compared
610 to global land, based on complementary data sources from space and surface observations, as well as the
611 CMIP6 climate models and ERA5 reanalysis. A further quantitative investigation of CREs at the TOA,
612 within the atmosphere, and at the surface is also conducted.

613 Comparisons between all-sky and clear-sky energy budgets indicate that the overall effects of clouds
614 greatly reduce the surface solar absorption by about 15.3% and enhance that within the atmosphere by 1.5%.
615 Compared to the global land energy budget estimates from Wild et al. (2015), for the SW budgets, notably
616 more atmospheric SW reflection of 5.2% but with a slightly less atmospheric SW absorption of 0.6% with
617 respect to their respective TOA incident solar radiation are estimated over East Asian land, possibly
618 indicating that the lower water vapor content effects due to TP overcompensate for the aerosol and cloud
619 effects over East Asian land. For the LW budgets, a substantially lower surface LW emission of around 25
620 W m^{-2} and smaller relative surface downward LW radiation of around 3.6% with respect to their respective
621 surface emissions can be noticed over East Asian land compared to global land, which possibly result from
622 the lower regional surface skin temperature, as well as the weaker greenhouse effect and fewer low clouds
623 mainly induced by the high altitude and thinner air over TP, thus leading to a higher percentage of regional
624 OLR of 2.7%.

625 The CREs over East Asian land are inferred through the energy budget differences between all-sky and
626 clear-sky conditions. The clouds reduce the solar absorption at the TOA by 46 W m^{-2} and enhance the TOA
627 thermal radiation by 24 W m^{-2} , respectively, leading to a TOA net CRE of -22 W m^{-2} , a more cooling effect
628 on the regional climate system than that over globe (-19 W m^{-2}). At the surface, the net CRE is estimated to
629 be -31 W m^{-2} according to less solar absorption of 51 W m^{-2} and more downward thermal radiation of 20 W
630 m^{-2} , indicative of larger cloud impacts on SW radiation. Within the atmosphere, the estimated net CRE is 9
631 W m^{-2} due to an increase of 5 W m^{-2} of solar absorption and 4 W m^{-2} of the net thermal radiation, respectively.
632 Compared to the global mean best estimates of CREs as introduced by Wild et al. (2019), relatively lower
633 East Asian land-mean best estimates of surface SW and LW CREs as well as the TOA LW CRE contribute
634 to the CRE differences between them.

635 On the whole, all the estimated land-mean energy balance components over East Asia in this study fall
636 within the uncertainty ranges of the CERES-derived assessments, except for the all-sky surface downward
637 LW radiation. More accurate and reliable datasets should be utilized to reduce the substantial uncertainties
638 in the regional energy balance estimates, particularly in the surface budgets, and more widespread temporal
639 and spatial representations of energy budget research are recommended for more comprehensive
640 comparisons in future. For example, newly published surface radiation products with high resolutions based
641 on satellite datasets (e.g., Letu et al., 2022; Xu et al., 2022) are expected to make sense in improving the
642 accuracy of the regional/global surface radiation budget studies.

643

644 *Acknowledgments.* This research was funded by the National Key Research and Development Program of
645 China (2017YFA0603502) and the Science and Technology Development Fund of CAMS
646 (2021KJ004&2022KJ019). The Global Energy Balance Archive (GEBA) is co-funded by the Federal
647 Office of Meteorology and Climatology Meteo Swiss within the framework of GCOS Switzerland.

648

649 *Data Availability.* The CERES SYN1deg data is available at [https://ceres-tool.larc.nasa.gov/ord-](https://ceres-tool.larc.nasa.gov/ord-tool/jsp/SYN1degEd41Selection.jsp)
650 [tool/jsp/SYN1degEd41Selection.jsp](https://ceres-tool.larc.nasa.gov/ord-tool/jsp/SYN1degEd41Selection.jsp); The AIRS data is accessible from
651 https://disc.gsfc.nasa.gov/datasets/AIRS3STM_006/summary?keywords=AIRS; The MODIS data is from
652 [https://ladsweb.modaps.eosdis.nasa.gov/archive/allData/61/MYD08_M3/?process=ftpAsHttp&path=allDat](https://ladsweb.modaps.eosdis.nasa.gov/archive/allData/61/MYD08_M3/?process=ftpAsHttp&path=allData%2f61%2fMYD08_M3)
653 [a%2f61%2fMYD08_M3](https://ladsweb.modaps.eosdis.nasa.gov/archive/allData/61/MYD08_M3/?process=ftpAsHttp&path=allData%2f61%2fMYD08_M3); The CloudSat data is from [http://www.cloudsat.cira.colostate.edu/data-](http://www.cloudsat.cira.colostate.edu/data-products/level-2b/2b-cwc-ro)
654 [products/level-2b/2b-cwc-ro](http://www.cloudsat.cira.colostate.edu/data-products/level-2b/2b-cwc-ro); The MERRA-2 dataset is obtained at
655 https://disc.gsfc.nasa.gov/datasets/M2IMNPANA_5.12.4/summary?keywords=merra-2. The ERA-Interim
656 is from <https://apps.ecmwf.int/datasets/data/interim-full-moda/levtype=sfc>.

657

658 *Author contributions.* HZ, MW, and QW proposed the main ideas of this study. QW designed and wrote the
659 manuscript. SY provided the homogenized ground-based surface solar radiation data. QC, XZ, and GS
660 contributed to the interpretation of the results. BX and YW assisted with the figures. All co-authors
661 participated in discussions and provided constructive suggestions.

662

663 *Competing interests.* The authors declare that they have no conflict of interest.

664

665 **References**

- 666 Boeke, R. C., and Taylor, P. C.: Evaluation of the Arctic surface radiation budget in CMIP5 models, *J. Geophys.*
667 *Res.-Atmos.*, 121, 8525–8548, <https://doi.org/10.1002/2016JD025099>, 2016.
- 668 Christensen, M. W., Behrangi, A., L'Ecuyer, T. S., Wood, N. B., Lebsock, M. D., and Stephens, G. L.: Arctic
669 observation and reanalysis integrated system: A new data product for validation and climate study, *B. Am.*
670 *Meteorol. Soc.*, 97, 907–916, <https://doi.org/10.1175/BAMS-D-14-00273.1>, 2016.
- 671 de Leeuw, G., Sogacheva, L., Rodriguez, E., Kourtidis, K., Georgoulias, A. K., Alexandri, G., Amiridis, V.,
672 Proestakis, E., Marinou, E., Xue, Y., and van der A, R.: Two decades of satellite observations of AOD over
673 mainland China using ATSR-2, AATSR and MODIS/Terra: data set evaluation and large-scale patterns, *Atmos.*
674 *Chem. Phys.*, 18, 1573–1592, <https://doi.org/10.5194/acp-18-1573-2018>, 2018.
- 675 Dolinar, E. K., Dong, X., Xi, B., Jiang, J. H., and Su, H.: Evaluation of CMIP5 simulated clouds and TOA
676 radiation budgets using NASA satellite observations, *Clim. Dynam.*, 44, 2229–2247,
677 <https://doi.org/10.1007/s00382-014-2158-9>, 2015.
- 678 Eyring, V., Bony, S., Meehl, G. A., Senior, C. A., Stevens, B., Stouffer, R. J., and Taylor, K. E.: Overview of the
679 Coupled Model Intercomparison Project Phase 6 (CMIP6) experimental design and organization, *Geosci.*
680 *Model Dev.*, 9, 1937–1958, <https://doi.org/10.5194/gmd-9-1937-2016>, 2016.
- 681 Fan, T., Zhao, C., Dong, X., Liu, X., Yang, X., Zhang, F., Shi, C., Wang, Y., and Wu, F.: Quantify contribution
682 of aerosol errors to cloud fraction biases in CMIP5 Atmospheric Model Intercomparison Project simulations,
683 *Int. J. Climatol.*, 38, 3140–3156, <https://doi.org/10.1002/joc.5490>, 2018.
- 684 Fasullo, J. T., and Trenberth, K. E.: The annual cycle of the energy budget. Part I: Global mean and land-ocean
685 exchanges, *J. Climate*, 21, 2297–2312, <https://doi.org/10.1175/2007JCLI1935.1>, 2008a.
- 686 Fasullo, J. T., and Trenberth, K. E.: The annual cycle of the energy budget. Part II: Meridional structures and

687 poleward transports, *J. Climate*, 21, 2313–2325, <https://doi.org/10.1175/2007JCLI1936.1>, 2008b.

688 [Ghan, S. J., Liu, X., Easter, R. C., Zaveri, R., Rasch, P. J., Yoon, J.-H., and Eaton, B.: Toward a minimal](#)
689 [representation of aerosols in climate models: Comparative decomposition of aerosol direct, semidirect, and](#)
690 [indirect radiative forcing. *J. Climate*, 25, 6461–6476, <https://doi.org/10.1175/JCLI-D-11-00650.1>, 2012.](#)

691 Gilgen, H., Wild, M., and Ohmura, A.: Means and trends of shortwave irradiance at the surface estimated from
692 global energy balance archive data, *J. Climate*, 11, 2042–2061, [https://doi.org/10.1175/1520-0442\(1998\)011<2042:MATOSI>2.0.CO;2](https://doi.org/10.1175/1520-0442(1998)011<2042:MATOSI>2.0.CO;2), 1998.

694 He, Y., Wang, K., Zhou, C., and Wild, M.: A revisit of global dimming and brightening based on the sunshine
695 duration, *Geophys. Res. Lett.*, 45, 4281–4289, <https://doi.org/10.1029/2018GL077424>, 2018.

696 Hersbach, H., Bell, B., Berrisford, P., Hirahara, S., Horányi, A., Muñoz-Sabater, J., Nicolas, J., Peubey, C., Radu,
697 R., Schepers, D., Simmons, A., Soci, C., Abdalla, S., Abellan, X., Balsamo, G., Bechtold, P., Biavati, G., Bidlot,
698 J., Bonavita, M., De Chiara, G., Dahlgren, P., Dee, D., Diamantakis, M., Dragani, R., Flemming, J., Forbes,
699 R., Fuentes, M., Geer, A., Haimberger, L., Healy, S., Hogan, R. J., Hólm, E., Janisková, M., Keeley, S.,
700 Laloyaux, P., Lopez, P., Lupu, C., Radnoti, G., de Rosnay, P., Rozum, I., Vamborg, F., Villaume, S., and
701 Thépaut, J.: The ERA5 global reanalysis, *Q. J. Roy. Meteor. Soc.*, 146, 1999–2049,
702 <https://doi.org/10.1002/qj.3803>, 2020.

703 Huang, G., Li, Z., Li, X., Liang, S., Yang, K., Wang, D., and Zhang, Y.: Estimating surface solar irradiance from
704 satellites: Past, present, and future perspectives, *Remote Sens. Environ.*, 233, 111371,
705 <https://doi.org/10.1016/j.rse.2019.111371>, 2019.

706 Kato, S., Rose, F. G., Rutan, D. A., Thorsen, T. J., Loeb, N. G., Doelling, D. R., Huang, X., Smith, W. L., Su, W.,
707 and Ham, S.: Surface Irradiances of Edition 4.0 Clouds and the Earth’s Radiant Energy System (CERES)
708 Energy Balanced and Filled (EBAF) data product, *J. Climate*, 31, 4501–4527, <https://doi.org/10.1175/JCLI-D-17-0523.1>, 2018.

709
710 Kim, B., and Lee, K.: Radiation component calculation and energy budget analysis for the Korean Peninsula
711 region, *Remote Sens.*, 10, 1147, <https://doi.org/10.3390/rs10071147>, 2018.

712 King, M. D., Platnick, S., Menzel, W. P., Ackerman, S. A., and Hubanks, P. A.: Spatial and temporal distribution
713 of clouds observed by MODIS onboard the Terra and Aqua satellites, *IEEE T. Geosci. Remote Sens.*, 51, 3826–
714 3852, <https://doi.org/10.1109/TGRS.2012.2227333>, 2013.

715 L’Ecuyer, T. S., Beaudoin, H. K., Rodell, M., Olson, W., Lin, B., Kato, S., Clayson, C. A., Wood, E., Sheffield,
716 J., Adler, R., Huffman, G., Bosilovich, M., Gu, G., Robertson, F., Houser, P. R., Chambers, D., Famiglietti, J.
717 S., Fetzer, E., Liu, W. T., Gao, X., Schlosser, C. A., Clark, E., Lettenmaier, D. P., and Hilburn, K.: The observed
718 state of the energy budget in the early twenty-first century, *J. Climate*, 28, 8319–8346,
719 <https://doi.org/10.1175/JCLI-D-14-00556.1>, 2015.

720 Lei, Y., Letu, H., Shang, H., and Shi, J.: Cloud cover over the Tibetan Plateau and eastern China: a comparison
721 of ERA5 and ERA-Interim with satellite observations, *Clim. Dynam.*, 54, 2941–2957,
722 <https://doi.org/10.1007/s00382-020-05149-x>, 2020.

723 [Letu, H., Nakajima, T. Y., Wang, T., Shang, H., Ma, R., Yang, K., Baran, A. J., Riedi, J., Ishimoto, H., and Yoshida,](#)
724 [M.: A new benchmark for surface radiation products over the East Asia–Pacific region retrieved from the](#)
725 [Himawari-8/AHI next-generation geostationary satellite. *B. Am. Meteorol. Soc.*, 103, E873–E888,](#)
726 [https://doi.org/10.1175/BAMS-D-20-0148.1, 2022.](#)

727 Li, J., L. F., Waliser, D. E., Stephens, G., Lee, S., L’Ecuyer, T., Kato, S., Loeb, N., and Ma, H.: Characterizing
728 and understanding radiation budget biases in CMIP3/CMIP5 GCMs, contemporary GCM, and reanalysis, *J.*
729 *Geophys. Res.-Atmos.*, 118, 8166–8184, <https://doi.org/10.1002/jgrd.50378>, 2013.

730 [Li, J., and Mao, J.: A preliminary evaluation of global and East Asian cloud radiative effects in reanalyses, *Atmos.*](#)
731 [and *Ocean. Sci. Lett.*, 8, 100–106, <https://doi.org/10.3878/AOSL20140093>, 2015.](#)

732 Li, J., Mao, J., and Wang, F.: Comparative study of five current reanalyses in characterizing total cloud fraction
733 and top-of-the-atmosphere cloud radiative effects over the Asian monsoon region, *Int. J. Climatol.*, 37, 5047–
734 5067, <https://doi.org/10.1002/joc.5143>, 2017.

735 [Li, Z., Niu, F., Fan, J., Liu, Y., Rosenfeld, D., and Ding, Y.: Long-term impacts of aerosols on the vertical](#)
736 [development of clouds and precipitation, *Nat. Geosci.*, 4, 888–894, <https://doi.org/10.1038/ngeo1313>, 2011.](#)

737 Liao, H., Chang, W., and Yang, Y.: Climatic effects of air pollutants over china: A review, *Adv. Atmos. Sci.*, 32,
738 115–139, <https://doi.org/10.1007/s00376-014-0013-x>, 2015.

739 Lin, B., Stackhouse Jr., P. W., Minnis, P., Wielicki, B. A., Hu, Y., Sun, W., Fan, T., and Hinkelman, L. M.:
740 Assessment of global annual atmospheric energy balance from satellite observations, *J. Geophys. Res.-Atmos.*,
741 113, <https://doi.org/10.1029/2008JD009869>, 2008.

742 Liu, Y., Bao, Q., Duan, A., Qian, Z. A., and Wu, G.: Recent progress in the impact of the Tibetan Plateau on
743 climate in China, *Adv. Atmos. Sci.*, 24, 1060–1076, <https://doi.org/10.1007/s00376-007-1060-3>, 2007.

744 Loeb, N. G., Doelling, D. R., Wang, H., Su, W., Nguyen, C., Corbett, J. G., Liang, L., Mitrescu, C., Rose, F. G.,
745 and Kato, S.: Clouds and the Earth’s Radiant Energy System (CERES) Energy Balanced and Filled (EBAF)

746 Top-of-Atmosphere (TOA) Edition-4.0 data product, *J. Climate*, 31, 895–918, [https://doi.org/10.1175/JCLI-](https://doi.org/10.1175/JCLI-D-17-0208.1)
747 [D-17-0208.1](https://doi.org/10.1175/JCLI-D-17-0208.1), 2018.

748 Mayer, M., Tietsche, S., Haimberger, L., Tsubouchi, T., Mayer, J., and Zuo, H.: An improved estimate of the
749 coupled Arctic energy budget, *J. Climate*, 32, 7915–7934, <https://doi.org/10.1175/JCLI-D-19-0233.1>, 2019.

750 Mercado, L. M., Bellouin, N., Sitch, S., Boucher, O., Huntingford, C., Wild, M., and Cox, P. M.: Impact of
751 changes in diffuse radiation on the global land carbon sink, *Nature*, 458, 1014–1017,
752 <https://doi.org/10.1038/nature07949>, 2009.

753 Ohmura, A.: Cryosphere During the Twentieth Century, *The state of the planet: frontiers and challenges in*
754 *geophysics*, Geophys. Monogr. Ser., 150, 239–257, <https://doi.org/10.1029/150gm19>, 2004.

755 Previdi, M., Smith, K. L., and Polvani, L. M.: How well do the CMIP5 models simulate the Antarctic atmospheric
756 energy budget? *J. Climate*, 28, 7933–7942, <https://doi.org/10.1175/JCLI-D-15-0027.1>, 2015.

757 Raschke, E., Kinne, S., Rossow, W. B., Stackhouse, P. W., and Wild, M.: Comparison of radiative energy flows
758 in observational datasets and climate modeling, *J. Appl. Meteorol. Clim.*, 55, 93–117,
759 <https://doi.org/10.1175/JAMC-D-14-0281.1>, 2016.

760 Simmons, A. J., Jones, P. D., Da Costa Bechtold, V., Beljaars, A. C. M., Källberg, P. W., Saarinen, S., Uppala, S.
761 M., Viterbo, P., and Wedi, N.: Comparison of trends and low-frequency variability in CRU, ERA-40, and
762 NCEP/NCAR analyses of surface air temperature, *J. Geophys. Res.-Atmos.*, 109,
763 <https://doi.org/10.1029/2004JD005306>, 2004.

764 [Stephens, G. L.: Cloud feedbacks in the climate system: A critical review, *J. Climate*, 18, 237-273,](https://doi.org/10.1175/JCLI-3243.1)
765 <https://doi.org/10.1175/JCLI-3243.1>, 2005.

766 Stephens, G. L., Li, J., Wild, M., Clayson, C. A., Loeb, N., Kato, S., L'Ecuyer, T., Stackhouse, P. W., Lebsock,
767 M., and Andrews, T.: An update on Earth's energy balance in light of the latest global observations, *Nat. Geosci.*,
768 5, 691–696, <https://doi.org/10.1038/ngeo1580>, 2012.

769 Tang, W. J., Yang, K., Qin, J., Cheng, C. C. K., and He, J.: Solar radiation trend across China in recent decades:
770 a revisit with quality-controlled data, *Atmos. Chem. Phys.*, 11, 393–406, [https://doi.org/10.5194/acp-11-393-](https://doi.org/10.5194/acp-11-393-2011)
771 [2011](https://doi.org/10.5194/acp-11-393-2011), 2011.

772 Thomas, C. M., Dong, B., and Haines, K.: Inverse modeling of global and regional energy and water cycle fluxes
773 using earth observation data, *J. Climate*, 33, 1707–1723, <https://doi.org/10.1175/JCLI-D-19-0343.1>, 2020.

774 Trenberth, K. E., Fasullo, J. T., and Balmaseda, M. A.: Earth's energy imbalance, *J. Climate*, 27, 3129–3144,
775 <https://doi.org/10.1175/JCLI-D-13-00294.1>, 2014.

776 Trenberth, K. E., Fasullo, J. T., and Kiehl, J.: Earth's global energy budget, *B. Am. Meteorol. Soc.*, 90, 311–324,
777 <https://doi.org/10.1175/2008BAMS2634.1>, 2009.

778 Trolliet, M., Walawender, J. P., Bourlès, B., Boilley, A., Trentmann, J., Blanc, P., Lefèvre, M., and Wald, L.:
779 Downwelling surface solar irradiance in the tropical Atlantic Ocean: a comparison of re-analyses and satellite-
780 derived data sets to PIRATA measurements, *Ocean Sci.*, 14, 1021–1056, [https://doi.org/10.5194/os-14-1021-](https://doi.org/10.5194/os-14-1021-2018)
781 [2018](https://doi.org/10.5194/os-14-1021-2018), 2018.

782 Urraca, R., Huld, T., Gracia-Amillo, A., Martinez-de-Pison, F. J., Kaspar, F., and Sanz-Garcia, A.: Evaluation of
783 global horizontal irradiance estimates from ERA5 and COSMO-REA6 reanalyses using ground and satellite-
784 based data, *Sol. Energy*, 164, 339–354, <https://doi.org/10.1016/j.solener.2018.02.059>, 2018.

785 [Wang, H., Zhang, H., Xie, B., Jing, X., He, J., and Liu, Y.: Evaluating the Impacts of Cloud Microphysical and](https://doi.org/10.1007/s00376-021-0369-7)
786 [Overlap Parameters on Simulated Clouds in Global Climate Models, *Adv. Atmos. Sci.*,](https://doi.org/10.1007/s00376-021-0369-7)
787 <https://doi.org/10.1007/s00376-021-0369-7>, 2021.

788 Wang, K.: Measurement biases explain discrepancies between the observed and simulated decadal variability of
789 surface incident solar radiation, *Sci. Rep.*, 4, 6144, <https://doi.org/10.1038/srep06144>, 2014.

790 Wang, K., Ma, Q., Li, Z., and Wang, J.: Decadal variability of surface incident solar radiation over China:
791 Observations, satellite retrievals, and reanalyses, *J. Geophys. Res.-Atmos.*, 120, 6500–6514,
792 <https://doi.org/10.1002/2015JD023420>, 2015.

793 Wang, Q., Zhang, H., Yang, S., Chen, Q., Zhou, X., Shi, G., Cheng, Y., and Wild, M.: Potential driving factors
794 on surface solar radiation trends over China in recent years, *Remote Sens.*, 13, 704,
795 <https://doi.org/10.3390/rs13040704>, 2021.

796 Wang, Y., Trentmann, J., Yuan, W., and Wild, M.: Validation of CM SAF CLARA-A2 and SARA-E surface
797 solar radiation datasets over China, *Remote Sens.*, 10, 1977, <https://doi.org/10.3390/rs10121977>, 2018.

798 Wang, Y., Wild, M., Sanchez-Lorenzo, A., and Manara, V.: Urbanization effect on trends in sunshine duration in
799 China, *Ann. Geophys.*, 35, 839–851, <https://doi.org/10.5194/angeo-35-839-2017>, 2017.

800 Wang, Y., and Wild, M.: A new look at solar dimming and brightening in China, *Geophys. Res. Lett.*, 43, 11,
801 711–777, 785, <https://doi.org/10.1002/2016GL071009>, 2016.

802 Wei, J., Peng, Y., Guo, J., and Sun, L.: Performance of MODIS Collection 6.1 Level 3 aerosol products in spatial-
803 temporal variations over land, *Atmos. Environ.*, 206, 30–44, <https://doi.org/10.1016/j.atmosenv.2019.03.001>,
804 2019.

805 Wild, M.: Progress and challenges in the estimation of the global energy balance, AIP Conference Proceedings,
806 1810, 20004, <https://doi.org/10.1063/1.4975500>, 2017a.

807 Wild, M.: Towards global estimates of the surface energy budget, *Curr. Clim. Change Rep.*, 3, 87–97,
808 <https://doi.org/10.1007/s40641-017-0058-x>, 2017b.

809 Wild, M.: The global energy balance as represented in CMIP6 climate models, *Clim. Dynam.*, 55, 553–577,
810 <https://doi.org/10.1007/s00382-020-05282-7>, 2020.

811 Wild, M., Folini, D., Hakuba, M. Z., Schär, C., Seneviratne, S. I., Kato, S., Rutan, D., Ammann, C., Wood, E. F.,
812 and König-Langlo, G.: The energy balance over land and oceans: an assessment based on direct observations
813 and CMIP5 climate models, *Clim. Dynam.*, 44, 3393–3429, <https://doi.org/10.1007/s00382-014-2430-z>, 2015.

814 Wild, M., Folini, D., Schär, C., Loeb, N., Dutton, E. G., and König-Langlo, G.: The global energy balance from
815 a surface perspective, *Clim. Dynam.*, 40, 3107–3134, <https://doi.org/10.1007/s00382-012-1569-8>, 2013a.

816 Wild, M., Folini, D., Schär, C., Loeb, N., Dutton, E. G., and König-Langlo, G.: A new diagram of the global
817 energy balance, AIP Conference Proceedings, 1531, 628–631, <https://doi.org/10.1063/1.4804848>, 2013b.

818 Wild, M., Grieser, J., and Schär, C.: Combined surface solar brightening and increasing greenhouse effect support
819 recent intensification of the global land-based hydrological cycle, *Geophys. Res. Lett.*, 35,
820 <https://doi.org/10.1029/2008GL034842>, 2008.

821 Wild, M., Hakuba, M. Z., Folini, D., Dörig-Ott, P., Schär, C., Kato, S., and Long, C. N.: The cloud-free global
822 energy balance and inferred cloud radiative effects: an assessment based on direct observations and climate
823 models, *Clim. Dynam.*, 52, 4787–4812, <https://doi.org/10.1007/s00382-018-4413-y>, 2019.

824 Wild, M., Hakuba, M. Z., Folini, D., Schär, C., and Long, C.: New estimates of the Earth radiation budget under
825 cloud-free conditions and cloud radiative effects, AIP Conference Proceedings, 1810, 90012,
826 <https://doi.org/10.1063/1.4975552>, 2017.

827 Wild, M., Ohmura, A., Gilgen, H., and Roeckner, E.: Validation of general circulation model radiative fluxes
828 using surface observations, *J. Climate*, 8, 1309–1324, [https://doi.org/10.1175/1520-0442\(1995\)008<1309:VOGCMR>2.0.CO;2](https://doi.org/10.1175/1520-0442(1995)008<1309:VOGCMR>2.0.CO;2), 1995.

829 Wu, G., Duan, A., Liu, Y., Mao, J., Ren, R., Bao, Q., He, B., Liu, B., and Hu, W.: Tibetan Plateau climate
830 dynamics: recent research progress and outlook, *Natl. Sci. Rev.*, 2, 100–116,
831 <https://doi.org/10.1093/nsr/nwu045>, 2015.

832 <https://doi.org/10.5194/essd-14-2315-2022>, 2022.

833 [Xu, J., Liang, S., and Jiang, B.: A global long-term \(1981–2019\) daily land surface radiation budget product from
834 AVHRR satellite data using a residual convolutional neural network, *Earth Syst. Sci. Data*, 14, 2315–2341,
835 <https://doi.org/10.5194/essd-14-2315-2022>, 2022.](https://doi.org/10.5194/essd-14-2315-2022)

836 Xu, X., Lu, C., Shi, X., and Gao, S.: World water tower: An atmospheric perspective, *Geophys. Res. Lett.*, 35,
837 <https://doi.org/10.1029/2008GL035867>, 2008a.

838 Xu, X., Zhang, R., Koike, T., Lu, C., Shi, X., Zhang, S., Bian, L., Cheng, X., Li, P., and Ding, G.: A new integrated
839 observational system over the Tibetan Plateau, *B. Am. Meteorol. Soc.*, 89, 1492–1496, 2008b.

840 Yang, S., Wang, X. L., and Wild, M.: Homogenization and trend analysis of the 1958–2016 in situ surface solar
841 radiation records in China, *J. Climate*, 31, 4529–4541, <https://doi.org/10.1175/JCLI-D-17-0891.1>, 2018.

842 Yang, S., Wang, X. L., and Wild, M.: Causes of dimming and brightening in China inferred from homogenized
843 daily clear-sky and all-sky in situ surface solar radiation records (1958–2016), *J. Climate*, 32, 5901–5913,
844 <https://doi.org/10.1175/JCLI-D-18-0666.1>, 2019.

845 You, Q., Liu, J., and Pepin, N.: Changes of summer cloud water content in China from ERA-Interim reanalysis,
846 *Global Planet. Change*, 175, 201–210, <https://doi.org/10.1016/j.gloplacha.2019.02.014>, 2019.

847 Zhang, H., Zhao, M., Chen, Q., Wang, Q., Zhao, S., Zhou, X., and Peng, J.: Water and ice cloud optical thickness
848 changes and radiative effects in East Asia, *J. Quant. Spectrosc. Radiat. Transf.*, 254, 107213,
849 <https://doi.org/10.1016/j.jqsrt.2020.107213>, 2020.

850